Global and Planetary Change 212 (2022) 103815

Contents lists available at ScienceDirect

Global and Planetary Change

journal homepage: www.elsevier.com/locate/gloplacha

Cenozoic weathering of fluvial terraces and emergence of biogeographic boundaries in Central Amazonia

Cécile Gautheron [a,*], André O. Sawakuchi [b], Marcio F. dos Santos Albuquerque [a,c], Cristiana Cabriolu [a], Mauricio Parra [b,d], Camilla C. Ribas [e], Fabiano N. Pupim [b,f], Stéphane Schwartz [g], Andrea K. Kern [b], Sebastián Gómez [b], Renato P. de Almeida [b], Adriana M.C. Horbe [c], Frederic Haurine [a], Serge Miska [a], Julius Nouet [a], Nathaniel Findling [g], Silvana Bressan Riffel [a,h], Rosella Pinna-Jamme [a]

[a] Université Paris-Saclay, CNRS, GEOPS, 91405, Orsay, France
[b] Instituto de Geociências, Universidade de São Paulo, Rua do Lago, 562, São Paulo, SP 05508-080, Brazil
[c] Instituto de Geociências, Universidade de Brasília, Campus Darcy Ribeiro, Brasília 70910-900, Brazil
[d] Instituto de Energia e Ambiente, Universidade de São Paulo, Av. Prof. Luciano Gualberto 1289, São Paulo, SP, Brazil
[e] Instituto Nacional de Pesquisas da Amazônia, Av. André Araújo 2936, Manaus, AM 69060-000, Brazil
[f] Universidade Federal de São Paulo, Departmento de Ciências Ambientais, Rua São Nicolau, 210, Diadema, SP, Brazil
[g] Univ. Grenoble Alpes, Univ. Savoie Mont Blanc, CNRS, IRD, Univ. Gustave Eiffel, ISTerre, 38000 Grenoble, France
[h] Instituto de Geociências, Universidade Federal do Rio Grande do Sul, Av. Bento Gonçalves, 9500, Porto Alegre, RS, Brazil

ARTICLE INFO

Editor: Zhengtang Guo

Keywords:
Weathering
Central Amazonia
Fluvial terraces
(U-Th)/he geochronology
Goethite and hematite

ABSTRACT

The study of paleofluvial dynamics is crucial to understand the role of rivers as biogeographic boundaries in Amazonia during the Cenozoic. In central Amazonia, Mesozoic and Cenozoic fluvial deposits - Alter do Chão, Iranduba and Novo Remanso Formations - host supergene iron oxides and record changes in the distribution of flooded and non-flooded (upland) environments. Geochronological data on these deposits are still scarce to constrain past landscape changes. Therefore, in this study we investigate iron oxides precipitated within weathering profiles developed on ancient fluvial terraces to access the interplay between flooded and non-flooded environments in central Amazonia. We aimed to trace the history of abandonment of alluvial plains and the subsequent weathering of lowland sediment deposits during the Cenozoic. We identified at least two main periods of iron oxide precipitation: (1) one starting before ~42 Ma and ending at ~18 Ma; and (2) a well-defined humid and weathering prone phase between ~8 and 1 Ma. Dominant goethite precipitation marks a major climatic shift towards more humid conditions from ~3 Ma. The increase in water discharge of the Negro and Solimões rivers possibly promoted fluvial incision and conversion of floodplains into long-lasting upland terrains as indicated by the development of lateritic weathering profiles. This major phase of upland expansion corroborates upland birds phylogenetic data, which indicate the emergence of a major biogeographic barrier in central Amazonia during late Pliocene/Pleistocene.

1. Introduction

The modern landscape of lowland Amazonia is shaped by extensive and diverse environments, largely influenced by the long-term dynamics of fluvial systems. Major Amazonian tributaries and their floodplains constitute geographical boundaries for the distribution of upland biota (Wallace, 1852; Ribas et al., 2012), suggesting that large rivers represent barriers for the dispersion of terrestrial species and thus often promote biotic diversification through vicariance (Cracraft et al., 2020). Major rivers also determine the distribution of species associated with seasonally flooded environments, which change the spatial continuity through time and drive their diversification (Thom et al., 2020). Lowland Amazonia in Brazil is lying over a thick succession of fluvial deposits, mostly pre-dating the Pleistocene and evidencing the presence of large riverine systems since at least the late Mesozoic (Cunha et al., 2007). These ancient fluvial networks are recorded in thick sandstone

* Corresponding author.
E-mail address: cecile.gautheron@universite-paris-saclay.fr (C. Gautheron).

https://doi.org/10.1016/j.gloplacha.2022.103815
Received 10 October 2021; Received in revised form 6 March 2022; Accepted 9 April 2022
Available online 14 April 2022

strata of the Alter do Chão Formation (Caputo et al., 1971), which crop out across eastern lowland Amazonia and are overlaid by late Cenozoic sediments of the Solimões Formation (Caputo et al., 1971) in western Amazonia and by the Iranduba and Novo Remanso Formations (Dino et al., 2012; Rozo et al., 2005) in central Amazonia.

A key region for the biological and geological evolution of lowland northern South America in central Amazonia is the confluence of the Negro and the Solimões (Amazon) rivers to form the largest river on Earth (Fig. 1). The confluence area forms the current biological boundary delimiting distributions of upland forest (Ribas et al., 2012; Boubli et al., 2015; Silva et al., 2019) and flooded forest species (Thom et al., 2020). In addition, it also marks the transition between the western lowlands, where a wide Cenozoic to Quaternary basin was filled with Andean-derived sediments, and the eastern Precambrian shields and Paleozoic-Mesozoic sedimentary cover (Caputo, 1984). In the subsurface, the boundary between the Paleozoic depocenters of the Solimões and Amazonas basins, named the Purus Arch (Caputo and Soares, 2016), has been related to a possible Cenozoic tectonic uplift that formed a water divide whose disruption during the late Cenozoic was necessary to shape the transcontinental Amazon River (Figueiredo et al., 2009). Bypassing of sediment across the Purus Arch has been explained as a consequence of either surface processes (increased discharge and sediment transport; Sacek, 2014), deep-seated processes (dynamic subsidence; Shephard et al., 2010) or a combination of both (Bicudo et al., 2020). The sedimentary record available to investigate this complex paleogeographic evolution in central Amazonia is represented by the Alter do Chão, Iranduba, and Novo Remanso Formations. These sediments are well exposed on the margins of the Negro, Solimões and Amazon rivers near the city of Manaus in northern Brazil (Fig. 1). These rivers also draw the boundaries of the Inambari, Jaú and Guiana biogeographic provinces (Silva et al., 2019; Cracraft et al., 2020) (Fig. 1).

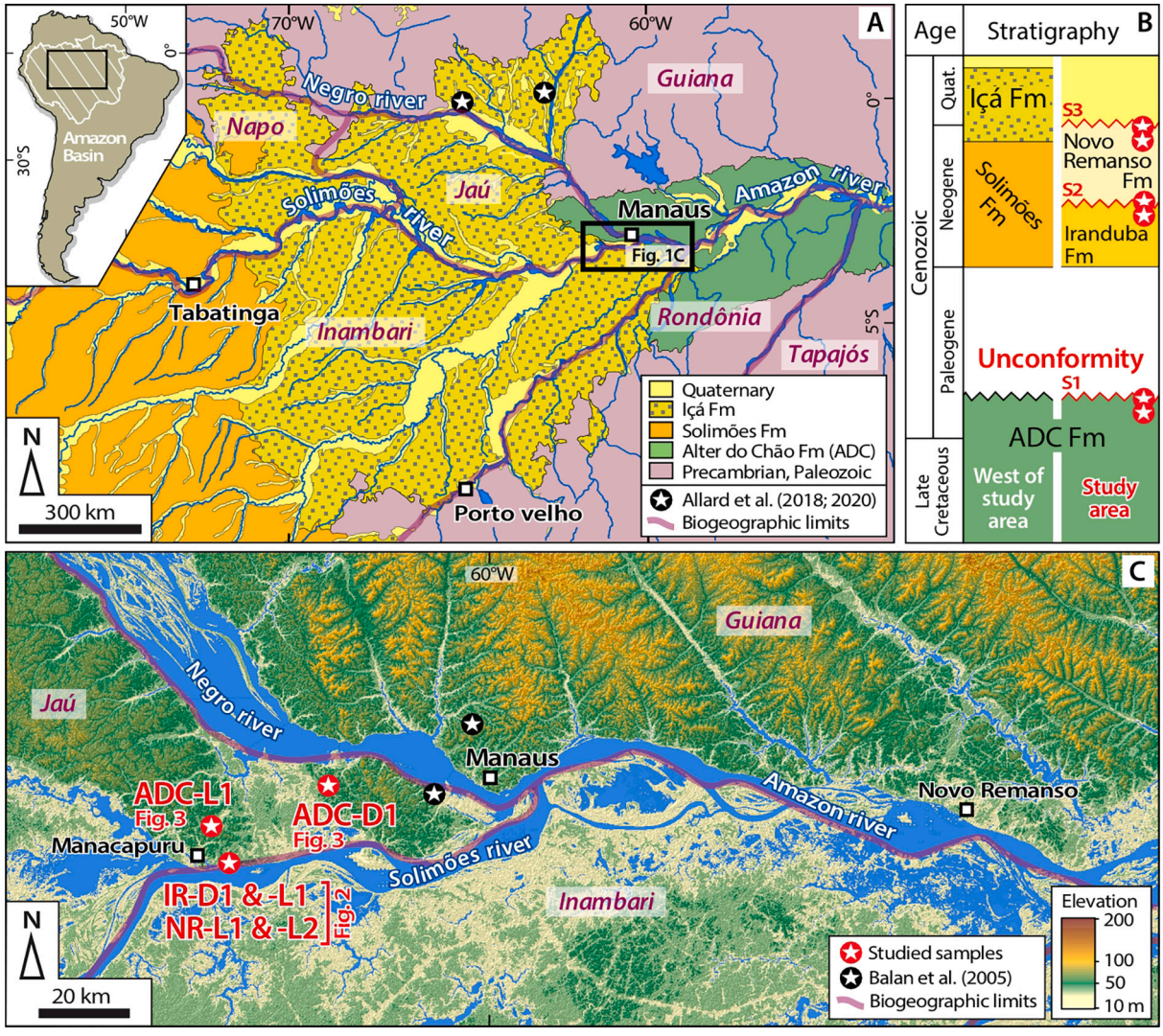

Fig. 1. Regional setting of central Amazonia. (A) Geological map (Shobbenhauns and Bellizzia, 2001) highlighting the spatial extent of the Içá, Solimões (Sol), and Alter do Chão (ADC) Formations; and the cratonic Precambrian (shield) and Paleozoic rocks (sedimentary cover). "Quaternary" represents undifferentiated sediments overlying any of the mentioned units. The spatial distribution of the Iranduba and Novo Remanso Formations have not been set yet and thus are not represented. The biogeographic provinces of Napo, Inambari, Jaú, Guiana, Rondônia and Tapajós have boundaries as defined in Ribas et al. (2012). Sites where electron paramagnetic resonance (EPR) or (U-Th)/He geochronological dating have been performed in supergene kaolinite and goethite respectively (black stars) developed on the Içá Formation (Allard et al., 2018; Allard et al., 2020) are also reported. (B) Simplified chronostratigraphic chart (Dino et al., 2012) representing S1, S2 and S3 paleosols levels interpreted as unconformities separating the Alter do Chão, Iranduba and Novo Remanso Formations. (C) Digital Elevation Model showing the sampling sites (red squares: this study; Black stars indicate EPR kaolinite dating on the Alter do Chão Formation (Balan et al., 2005) along the fluvial terraces at the margins of the Solimões River. Image from Shuttle Radar Topography Mission data (SRTM 3 arc-seconds, earthexplorer.usgs.gov). (For interpretation of the references to color in this figure legend, the reader is referred to the web version of this article.)

The fluvial deposits of upland areas in central Amazonia show remarkable zones rich in supergene iron oxides (i.e., hematite and goethite) that have precipitated in lateritic duricrusts and iron-enriched horizons within the sedimentary strata. Iron-lateritic duricrusts can only be formed through the combination of intense chemical weathering and slow erosion (Retallack, 2010), implying tropical climatic conditions, the release of chemical elements from the parent rock, and the precipitation of secondary supergene mineral phases (e.g., goethite, hematite, and kaolinite) during the lateritization process (Nahon, 2003; Nahon and Tardy, 1992). During weathering processes, soluble Fe^{2+} is enriched in the water table, and under redox condition is oxidized to Fe^{3+} and precipitates as iron-oxides. Goethite precipitates in humid conditions, whereas it can be transformed into hematite by dehydration if humidity is reduced (e.g., Nahon and Tardy, 1992). In addition, the hematite/goethite ratio could be used as a proxy for rainfall, and thus change in the environmental condition (Zhao et al., 2017). The iron-lateritic duricrusts are formed at the surface through intense weathering, which means that the laterite should be in an upland position above the local base level. Associated with lateritic profile development, goethite can also precipitate in the non-saturated zone above the water table (e.g., Tardy, 1992), forming iron-rich levels. Whereas iron-lateritic duricrust is a direct weathering product associated with the lateritization process, iron-enrichment levels are the Fe-rich water table that does not precipitate necessary in situ (Eze et al., 2014; Nahon, 2003; Nahon and Tardy, 1992; Tardy, 1992). The distances of subsurface transport of iron-rich solutions are not well known, however it is important to distinguish between possible conditions of iron-oxides formation. Thus, the supergene iron oxides within ancient fluvial deposits record the weathering history of Amazonian lowlands and can be applied to constrain both the ages of sediment deposition or erosion and climate conditions.

Here, we use the (U-Th)/He geochronological dating method to study authigenic supergene goethite and hematite from three sites in central Amazonia (Fig. 1). We aim to determine the history of weathering, the changes in climatic conditions, and the conversion of Amazonian alluvial plains into uplands during the Cenozoic. Authigenic precipitation of goethite and hematite in a weathering profile provides a minimum age for sediment deposition. Thus, the (U-Th)/He results presented here allow us to reconstruct past landscapes of flooded and non-flooded environments throughout the Cenozoic and discuss the role of river barriers driving Amazonian biotic diversification and biogeographic patterns.

2. Sedimentological and weathering contexts

The Alter do Chão, Iranduba, and Novo Remanso Formations crop out on the northern margin of the Solimões-Amazon River (Fig. 1) mainstem around Manaus (Fig. 1). The Alter do Chão Formation is broadly exposed east of the Purus Arch, in the Amazonas Sedimentary Basin while the Iranduba and Novo Remanso Formations have been described only in the western part (Fig. 1) and chronological information to define boundaries are still scarce. Especially, detailed mapping of the Iranduba and Novo Remanso Formations is limited, and the stratigraphic correlation is complex due to the absence of unambiguous stratigraphic markers. In central Amazonia, between the cities of Manacapuru and Manaus (Fig. 1), outcrops assigned to the Alter do Chão, Iranduba, and Novo Remanso Formations show remarkable zones rich in supergene iron oxides. These iron-rich layers have been used to define the regional stratigraphic boundaries among the Alter do Chão, Iranduba, and Novo Remanso Formations and overlying undifferentiated sediments that have been informally named as S1, S2, and S3 (Abinader, 2008; Dino et al., 2012) (Fig. 1B). Abinader (2008) proposes that the weathering event leading to the formation of the S1 paleosol started before the deposition of the Iranduba Formation, with a supposed Miocene age, but for some localities the S1 level is possibly correlated with the S2 iron-rich level. Both S1 and S2 levels correspond to a lateritic iron duricrust. In contrast, the S3 paleosol corresponds to an iron-enrichment level, i.e. petroplinthite (Eze et al., 2014). The Fe-rich supergene levels are associated with intense chemical weathering and precipitation, dissolution and reprecipitation episodes (e.g., Monteiro et al., 2014).

Available paleocurrent and sediment provenance data from the Alter do Chão Formation, although limited, point to west-southwestward flow (Abinader, 2008) and a cratonic provenance (Mendes et al., 2015), suggesting an axial east-west river (Fig. S1 and Table S3). A switch to a southeastward flow is described in the younger Iranduba and Novo Remanso Formations (Rozo et al., 2005; Abinader, 2008; Dino et al., 2012). Two detrital zircon samples from the Novo Remanso and Iranduba Formations with similar U/Pb age distributions dominated by 1.85 to 1.9 Ga zircons (Mapes, 2009) point to a similar sediment source for both Neogene units. This signature resembles the ages of the nearby Ventuari-Tapajós Province, present in the north and northwest areas (Tassinari and Macambira, 1999), suggesting drainages with south or southeastward flow. A similar source for both units is also suggested by heavy mineral assemblages dominated by zircon, tourmaline, and rutile (Abinader, 2008), although heavy minerals assemblages could be affected by the intense weathering. Minor populations of zircons with ages resembling those of the 1.8–1.55 Ga Rio Negro-Juruena Province (Tassinari and Macambira, 1999), and the 2.2–1.95 Ga Maroni Itacaiúnas Province (Tassinari and Macambira, 1999), which crop out to the northwest and north of the study area respectively, further support the interpretation of a northwestern, local, cratonic source. This interpretation agrees with northwestern paleocurrent data measured in the study area (Fig. S1 and Table S3).

The deposition ages of the fluvial sand-dominated successions in the study area are poorly constrained due to the absence of ash layers and the lack of paleontological material. Current biostratigraphical information is based on palynological data from the Alter do Chão and Novo Remanso Formations limited to only a few samples. For the Iranduba Formation, no biostratigraphical data exist in the literature. For the Alter do Chão Formation, palynological data have been retrieved from drilled core material several hundred-meters deep (Daemon and Contreiras, 1971; Dino et al., 1999; Dino et al., 2012), where assemblages contain typical markers for a late Cretaceous age. The Alter do Chão sequence is best described in the Petrobras drilling 1-NO-1-AM (Nova Olinda), where depositional sequences of an Aptian and Cenomanian ages are divided by an unconformity (Dino et al., 1999). However, no suitable sample for biostratigraphy could be analyzed from the top of the Alter do Chão Formation, fostering the discussion of a Paleogene (ANA, 2015) or Neogene (Caputo, 2009) upper boundary. Finally, the biostratigraphic information on the Novo Remanso Formation is based on two outcrops along the Solimões River (Dino et al., 2012; Guimarães et al., 2015) and three outcrops along the Uatumã River (Soares et al., 2015), which all agree on a Neogene depositional age. While most studies assign a middle Miocene palynozone, Guimarães et al. (2015) describe a wide age range from the middle Miocene to the Pliocene using a quantitative biostratigraphic approach despite similar palynological assemblages. Due to the paucity of palynological samples in central Amazonia, as well as the absence of local constraints, discussion on the boundaries of palynological biozones is still ongoing. A detailed review of the palynological ages of the Alter do Chão and Novo Remanso Formations is summarized in the supplementary section.

3. Materials and methods

3.1. Sampling details

Samples of iron-lateritic duricrusts (D), iron-enrichment levels (L), and sandstones were collected during field trips in 2017 and 2018 (Table 1; Fig. 1B).

The collected samples are from exposed strata of Alter do Chão (ADC), Iranduba (IR), and Novo Remanso (NR) Formations that represent the host material (Table 1). Field views of the studied outcrops are

Table 1
Samples description, location and mineral phase quantifications deduced from the X-ray diffraction (XRD) spectrum on bulk samples. *

Sample codes	Field sample codes	Latitude (°S)	Longitude (°W)	Elevation (m)	Sample description and formation	Quartz (%)	Goethite (%)	Hematite (%)	Kaolinite (%)
ADC-L1	ALC56A	3°13′41.1”	60°34′01.3”	28	Iron enrichment level on Alter do Chão Formation	0	100	0	0
ADC-D1	ALC58	3°09′24.6”	60°20′16.5”	33	Lateritic profile with 1 m thick iron-lateritic duricrust on Alter do Chão Formation. Columnar aspect with vermiform texture, where the reddish framework/matrix is composed of hematite and the voids/cavities are mostly filled by kaolinite with goethite. Two specimens (ADC-D1#1 and ADC-D1#2) were collected.	33	40	20	7
NR-L1	ALC57A	3°18′27.5”	60°31′59.5”	26	Iron enrichment level (petroplinthite) between Novo Remanso Formation sandstone and Barro Branco* clay (~1 m thick)	23.6	66.6	0	9.5
NR-L2	ALC57B	3°18′27.5”	60°31′59.5”	25	Iron enrichment level (petroplinthite) on Novo Remanso sandstone (15 cm thick)	31.8	20.2	18.4	28.7
IR-D1	ALC44E	3°18′27.5”	60°31′59.5”	16	Iron-lateritic duricrust developed on Iranduba. Columnar aspect with vermiform texture.	27.4	38.6	25.5	6.5
IR-L1	ALC44F	3°18′27.5”	60°31′59.5”	15	Iron enrichment level in Iranduba reddish sandstone (10 cm thick)	51.9	24.6	13.4	10.1

* Fine-grained sediments on top of the Novo Remanso Formation are informally named as “Barro Branco clay”.

presented in Figs. 2 and 3.

We collected iron-rich samples along three outcrops, including two samples of iron-lateritic duricrusts (IR-D1 and ADC-D1) and four iron-enrichment levels (IR-L1, ADC-L1, NR-L1, and NR-L2) from well-exposed sections of the host rock (Table 1 and Fig. 1). The ferruginization levels developed on top of the Novo Remanso strata (NR-L1 and NR-L2) is a petroplinthite (Eze et al., 2014), whereas the levels developed in the Iranduba and Alter do Chão Formations (IR-L1 and ADC-L1) are linked with the non-saturated zone above the water table. The ADC-L1 and ADC-D1 samples were collected in road construction outcrops. Apart from samples ADC-L1 and ADC-D1, all samples were taken along an 11 m–thick profile cropping out in the left bank of the Solimões River as shown in Fig. 2. Other descriptions of these sites can be found in Dino et al. (2012). Samples IR-L1, NR-L1, and NR-L2 are iron-oxide enrichment levels in which goethite mainly fills the porosity among quartz grains. On the other hand, samples IR-D1 and ADC-D1 are iron-lateritic duricrusts formed on top of a lateritic profile developed on the Iranduba and Alter do Chão Formations, as already described by Dino et al. (2012). Two blocks of ADC-D1 iron-lateritic duricrust were collected ~27 km to the northeast (Fig. 1), whereas ADC-L1 is a pure iron-enrichment level above an iron-lateritic duricrust developed on the Alter do Chão Formation 10 km to the north from location of samples IR-D1, IR-L1, and NR-L1, NR-L2 (Fig. 1).

3.2. Sample preparation

The iron oxides and hydroxides were extracted from the rocks using two methodologies. For the iron-lateritic duricrust sample (IR-D1) and the iron-enrichment level samples (IR-L1, NR-L1 and NR-L2), we applied a protocol where the iron oxides fragments were retrieved by crushing, sieving, and cleaning procedures. Firstly, hand specimens were crushed and sieved to isolate the fraction between 63 and 500 μm. Subsequently, the lighter mineral fraction was removed by panning. We choose to retrieve the iron oxides and hydroxides grains by crushing because of the small size of the goethite and hematite grains (<1 mm). For the iron-lateritic sample ADC-D1, we obtained slices from the iron-lateritic duricrust blocks in order to manually extract iron oxides and hydroxides based on color differences using a microdrill. This protocol allows to identify different generations of supergene minerals and to select them for mineralogical and (U-Th)/He dating. Grains with metallic luster were selected for mineralogical characterization and (U-Th)/He measurement. However, optical differentiation between goethite and hematite is unsuitable especially if the grains are mixed mineralogical phases. Thus, the type of selected oxides and hydroxides fragments for (U-Th)/He dating is not exactly known for samples where the bulk mineralogical results present hematite/goethite mixed mineralogy. Interpretation of hematite and goethite (U-Th)/He will be similar but mixing of populations can lead to (U-Th)/He age dispersion if the hematite and goethite precipitated in different time range as shown by Monteiro et al. (2014) and Heller et al. (2022). However, for ADC-D1 sample, the mineralogy of the iron-oxides or hydroxides generations was investigated by X-ray diffraction (XRD) analysis. In the following, for simplicity, the term iron-oxides will be used to refer to the selected samples rather than iron oxides and hydroxides. This information is crucial as goethite and hematite precipitate in iron-lateritic duricrusts during different geochemical conditions (Zhao et al., 2017; Cornell and Schwertmann, 2004).

3.3. Petrological, mineralogical and crystallographic descriptions

The petrological, mineralogical, and crystallographic properties of samples ADC-L1, ADC-D1, NR-L1, NR-L2, IR-D1, and IR-L1 were characterized using optical microscopy and scanning electron microscopy (SEM), and XRD analyses. Petrological observations were performed on polished thin sections using reflected light to identify the iron oxides and hydroxides characteristics and their relationship with other minerals for samples NR-L1, NR-L2, IR-D1, and IR-L1 (Fig. 4). Sample ADC-L1 is composed of pure goethite and no thin section has been made for this sample. For sample ADC-D1, the two sample slices enabled identification of Fe-minerals generations and mineralogical analysis (Fig. 5).

The XRD analyses were performed on bulk sample fractions in order to identify the main minerals and to select iron oxides and hydroxides types (i.e. goethite, hematite) for the (U-Th)/He dating. The XRD analyses in bulk samples (IR-D1, IR-L1, NR-L1, NR-L2) were performed using a Bruker D8 powder diffractometer equipped with a SolXE Si(Li) solid-state detector from Baltic Scientific Instruments, using CuKα_1 + 2 radiation at the Institut des Sciences de la Terre (France). To obtain well-defined peaks, the analysis was set with an acquisition time of 8 h per pellet to reduce the fluorescence interferences of iron-oxides samples. The XRD analysis of the two remaining samples (ADC-L1, ADC-D1) was carried out on 2 g of material on small grains powder using a PANalytical X’pert Pro diffractometer with a Cupper target anode, at GEOPS laboratory (France). The identification of the mineral phases was performed on the PANalytical HighScore software followed by a Rietveld refinement for quantification (McCusker et al., 1999). The associated error bars are 1% for well-crystallized phases (goethite, hematite, and

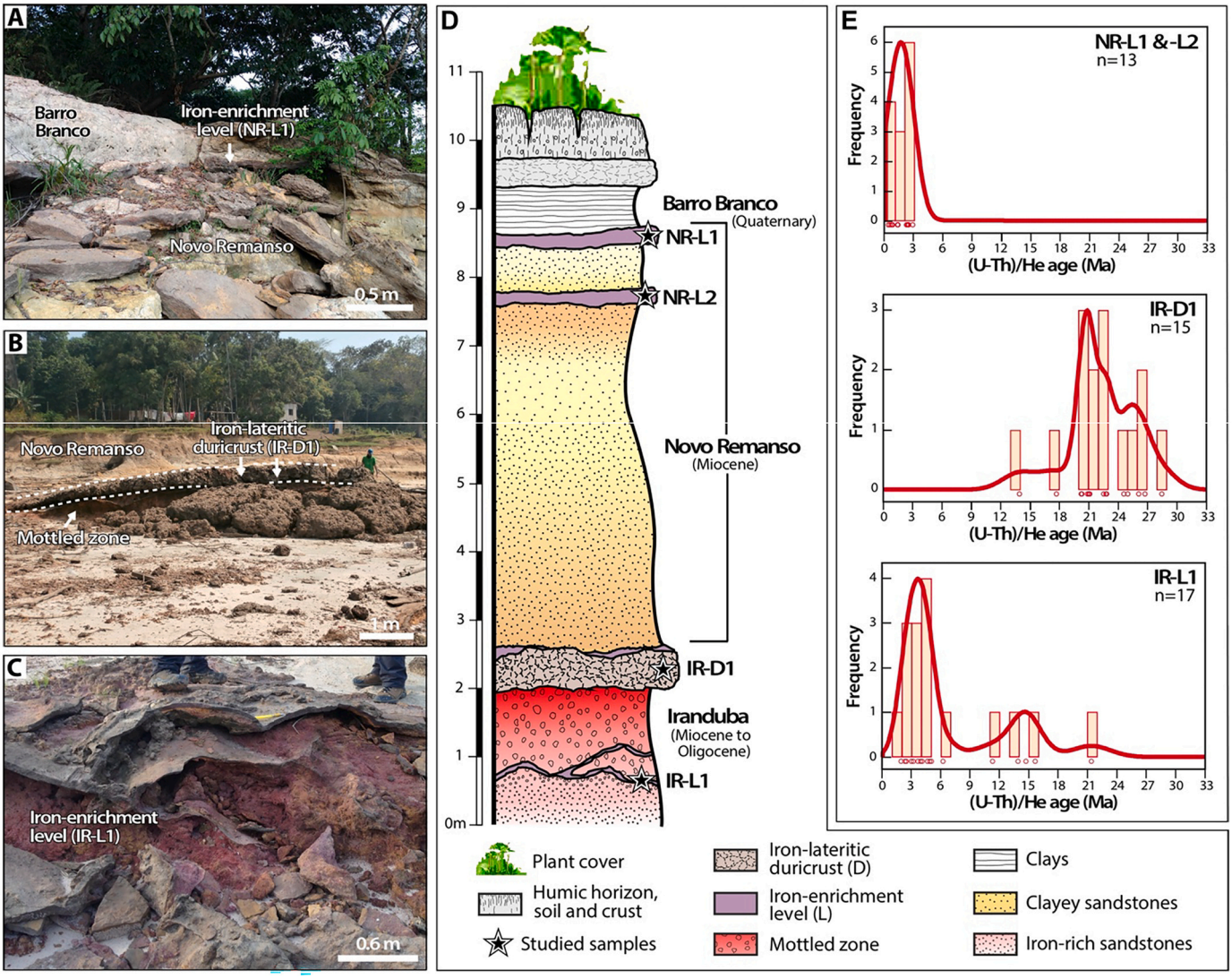

Fig. 2. Studied sections on a bank of the Solimões River (see location on Fig. 1) and their age distributions. (A) (B) and (C) Outcrop pictures and samples descriptions. (D) Schematic log of the studied outcrops with supposed sediment deposition ages from the literature and location of samples IR-D1, IR-L1, NR-L1 and NR-L2. (E) Histograms and probability curves of (U-Th)/He ages acquired for samples NR-L1 & L2, IR-D1 and IR-L1. Fine-grained sediments on top of the Novo Remanso Formation are informally named as "Barro Branco" clay. Iron-oxides (U-Th)/He age histograms were performed using the RadialPlotter program (Vermeesch, 2009).

quartz) and around 5% for kaolinite.

Semi-quantitative SEM analyses and backscattered electrons (BSE) imaging of similar iron-oxides grains to those selected for (U-Th)/He dating were performed on carbon-coated grains using a conventional TESCAN VEGA-3 SEM operated at low kW and equipped with a RAY-SPEC EDS detector (SSD 30 mm2152) at the Institut des Sciences de la Terre (France). SEM images performed on IR-L1 and NR-L1 samples are presented in Fig. S3. As the samples were crushed and sieved, the type of iron-oxides mineralogy is not known, even if two different generations (that can be of similar mineralogy) can be identified for the IR-L1 sample. In addition, SEM was also performed on slices of ADC-D1 using a Phenom X Pro SEM and a charge compensation sample holder at GEOPS laboratory (France). Pictures were produced in the imaging mode at an acceleration voltage of (5–10-15) kV. Spot analyzes of semi-quantitative elemental compositions were measured through energy dispersive X-ray spectrometry (EDS) with the analysis mode at an acceleration voltage of 15 kV and an accumulation time of 30 s.

3.4. (U-Th)/He dating

The principle of the (U-Th)/He dating method relies on the ^{4}He production, ejection and accumulation inside the crystal structure during the alpha decay of the radioactive ^{235}U, ^{238}U, ^{232}Th and ^{147}Sm elements (Farley, 2002). In supergene goethite and hematite, different amounts of U and Th are incorporated at some ppm level in the crystal structure, reflecting oxide-reduction conditions and weathering intensity as U is soluble and Th insoluble. The raw (U-Th)/He age is then calculated using the He and U-Th-Sm contents without a correction for alpha ejection, as the mean alpha stopping distance of the ejected He in iron oxides and hydroxides ranges from 14 to 16 μm (Ketcham et al., 2011), which is small compared to the sample size (circa 0.3–1 mm before disaggregation during the sample preparation). On the other hand, He can be lost by diffusion due to the polycrystalline nature of the millimetric samples (e.g., Shuster et al., 2005; Vasconcelos et al., 2013; Allard et al., 2018). A loss of between 5 and 30% of He by diffusion has been generally estimated for goethite (e.g. Shuster et al., 2005; Vasconcelos et al., 2013; Hofmann et al., 2017), and around 5% for hematite (Farley, 2018), but a mean loss of 10% and a 10% error is generally admitted and used in this study. As the selected iron-oxides aliquots can be made of crystallites precipitated from fluids of different U-Th content and age, possible (U-Th)/He age dispersion can reflect the dynamics of the weathering system. As the age is obtained using the bulk He, U-Th

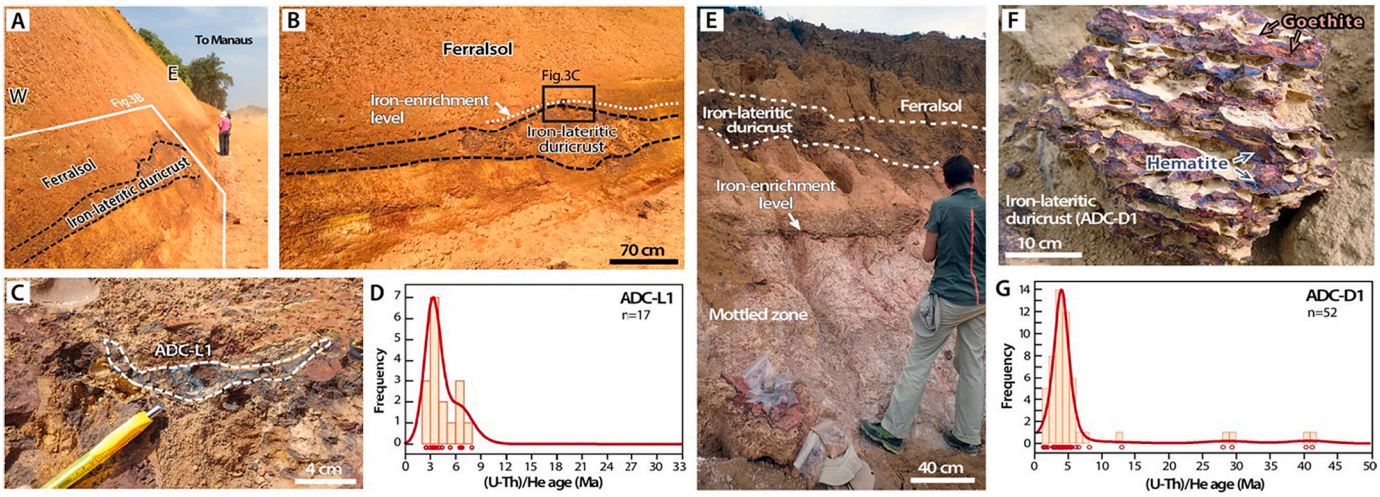

Fig. 3. Outcrops and characteristics of samples ADC-L1 and ADC-D1 developed on the Alter do Chão Formation. (A) General view of the ADC-L1 outcrop. (B) Zoom view on the sampled zone. An iron-lateritic duricrust and an iron-enrichment level are also identified. (C) Iron-enrichment level ADC-L1 sample. (D) Histograms and probability curves of (U-Th)/He ages acquired on sample ADC-L1. (E) General view of the ADC-D1 outcrop showing, from top to bottom, the Ferralsol, iron-lateritic duricrust and mottled zone, which represent the typical sequence of a lateritic profile (Nahon and Tardy, 1992; Tardy, 1992). An iron-enrichment level (not studied here) is also observed in the mottled zone. (F) Collected iron-lateritic duricrust block with typical reddish color associated with hematite and goethite precipitation. (G) Histograms and probability curve of (U-Th)/He ages acquired on sample ADC-D1.

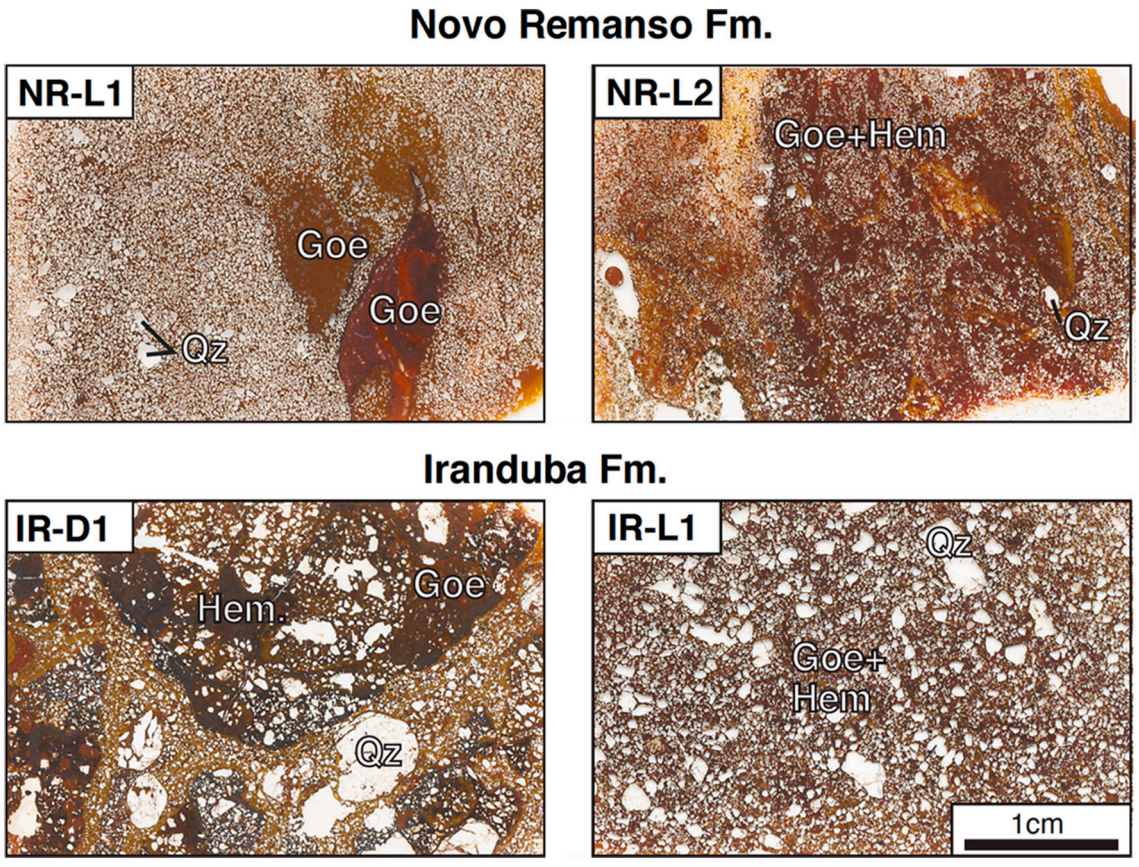

Fig. 4. Optical micro-photographs of thin sections of the NR-L1, NR-L2, IR-D1 and IR-L1 samples. Goethite (Goe), hematite (Hem), and quartz (Qz) occur in all samples but with different proportions. Goethite and hematite are differentiated by colors. Deep red is characteristic of hematite, orange of goethite, and yellow/orange of Al-goethite. (For interpretation of the references to color in this figure legend, the reader is referred to the web version of this article.)

and Sm contents measured on the aliquot, the age will reflect the mixture of the different phases. Because iron-oxides are opaque minerals, the identification of different populations can be made using the aliquots color and luster and by studying in detail the sample mineralogy and geochemistry. Several authors have already investigated the origin of (U-Th)/He geochronological age significance of supergene hematite and goethite, by deciphering the oxides populations with the U and Th content variations within the aliquots (e.g., Vasconcelos et al., 2013;

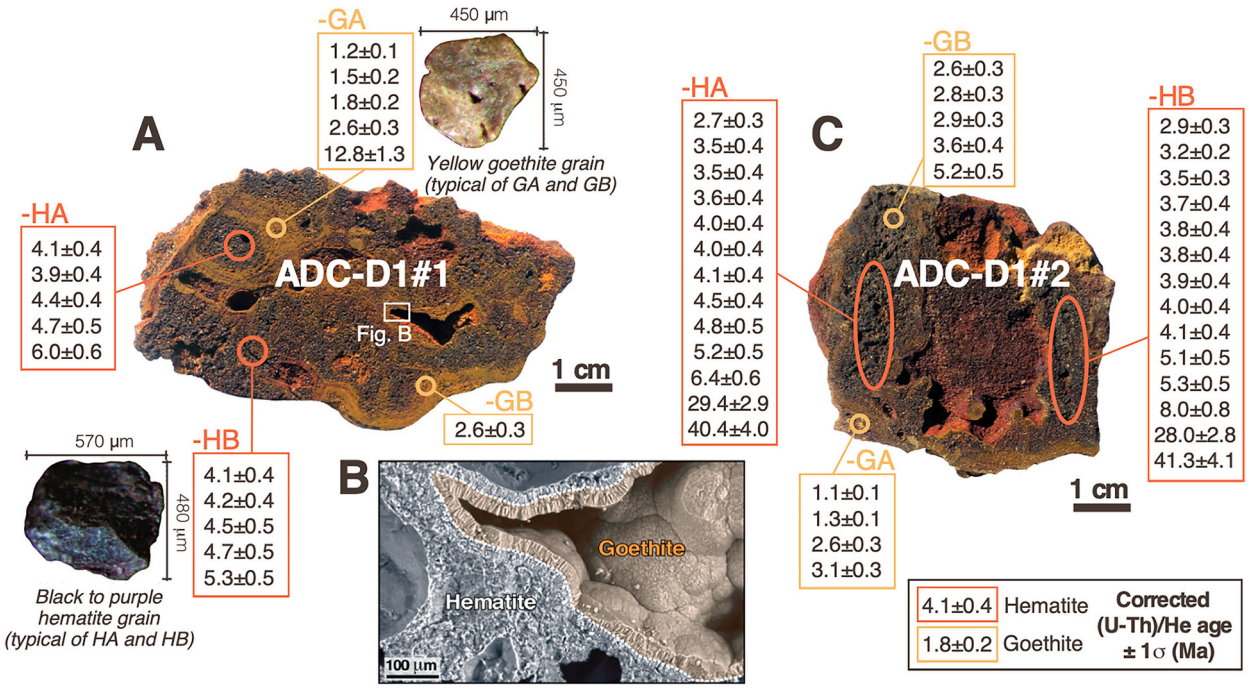

Fig. 5. ADC-D1 iron-lateritic duricrust supergene mineralogy. (A) Photography of the ADC-D1#1 sample block showing the two secondary supergene products (hematite and goethite). (B) SEM photography revealing at a smaller scale two mineralogical phases. (C) Photography of the ADC-D1#2 sample block. Corrected (U-Th)/He ages are reported for each manually extracted fraction based on color differences. -HA and -HB are two hematite rich zones and -GA and -GB are two goethite rich zones of both ADC-D1#1 and ADC-D1#2 samples blocks.

Monteiro et al., 2014; Riffel et al., 2016: Heller et al., 2022).

When possible, more than ten single iron-oxides fragments, ~100–600 µm long, were selected under a binocular microscope, and each one was encapsulated into a weighed niobium (Nb) tube and weighed again to determine the aliquot mass, which ranges from 13 to 174 µg. Only three analyses were performed for the NR-L1 sample due to the lack of datable grains. The He content was measured at GEOPS laboratory (France). Each encapsulated iron-oxides fragment was degassed using a He extraction line coupled with a quadrupole mass spectrometer referred to as the He line, or with a He extraction line coupled with a homemade revised VG5400 magnetic sector mass spectrometer, referred to as the VG line (Gautheron et al., 2021). After degassing, the samples encapsulated into the Nb tubes were extruded from the tube directly into 5 mL Teflon-capped vials for complete dissolution. Firstly, 50 µL of 5 N HNO_3 containing a known amount of ^{235}U, ^{230}Th, and ^{149}Sm were introduced in each vial followed by 400 µL of 30% HCl, and a few drops of 38% HF. The vials were closed and heated up to 100 °C overnight. The solutions were evaporated at 100 °C to concentrate the sample. If the sample was not completely dissolved, the procedure of adding HCl and HF was repeated. Secondly, 5 mL of 5 N HNO_3 was added to the final solution and heated for 1 h at 100 °C. The solution was diluted with 1 N HNO_3. Eventually, U, Th, and Sm measurements were undertaken by using an ELEMENT XR ICPMS at the GEOPS laboratory and a quadrupole Agilent 7900 ICP-MS at the IPGP (France). Durango apatite was regularly analyzed to check the (U-Th)/He analysis reproducibility (see Gautheron et al., 2021 for additional details).

4. Results

4.1. Petrological and mineralogical results

XRD and SEM analyses show that the samples contain quartz, goethite, hematite, and kaolinite in different proportions (Table 1 and Fig. 6).

Two iron-oxides types are recognized in thin sections of samples NR-L1, NR-L2, IR-D1 and IR-L1 (Fig. 4), and on the slices performed on sample ADC-D1 (Fig. 5), whereas, as ADC-L1 sample is a pure goethite (Fig. 3). In detail, a first reddish hematite generation coats the detrital quartz grains in sample ADC-D1 (Fig. 5), whereas a second yellow-orange goethite generation forms botryoidal structures (Fig. 5). Goethite is the main iron-oxide phase of samples ADC-L1 and NR-L1, whereas for other samples goethite and hematite are present in similar proportions. In some samples, an intergrowth of iron-oxides is observed at different scales as shown in Figs. 5B and 7.

All these observations demonstrate that the studied samples record different stages of weathering revealed by the crystallization of varied generations of goethite and hematite.

4.2. Goethite and hematite (U-Th)/He ages

A total of 104 goethite and hematite (U-Th)/He dates were acquired from six samples, which include four samples (IR-L1, IR-D1, NR-L1, and NR-L2) from the 11-m thick profile in the northern margin of the Solimões River (Fig. 2), and two samples (ADC-D1 and ADC-L1) from two locations situated few km to the north, in the interfluve of the Solimões and Negro rivers (Fig. 3).

All (U-Th)/He ages for the two iron-lateritic duricrusts (IR-D1 and ADC-D1) range from 41.3 ± 4.1 to 1.1 ± 0.1 Ma, whereas the (U-Th)/He ages for all iron-enrichment levels samples (IR-L1, ADC-L2, and NR-L1-L2) range from 21.4 ± 1.9 to 0.3 ± 0.01 Ma (Table 2; Figs. 2 and 3). However, as the ages can bear a complex signal, the relationship between (U-Th)/He age and contents of U and Th (Sm contribution to the He budget is almost negligible) can be further investigated using a He-U-Th ternary diagram in order to access age distribution patterns and dispersion (Fig. 8). The ternary diagram presents the (U-Th)/He data in a way that gives the uncorrected (U-Th)/He ages, with the He, U and Th concentrations variation for the different data. We represented separately the (U-Th)/He data for the different iron lateritic duricrusts and Fe-enrichment levels developed over Iranduba and Alter do Chão

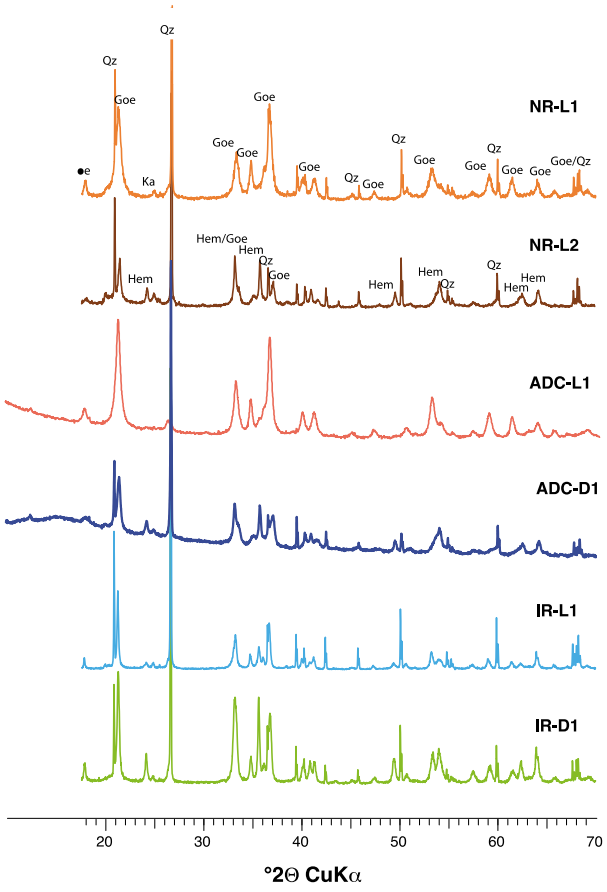

Fig. 6. X-ray diffractograms of the bulk analyzed samples. Ka: kaolinite; Goe: goethite, Hem: hematite, Qz: quartz. Kaolinite is a minor component in all samples, except for ADC-L2 that is made of pure goethite.

sedimentary strata with the identified mineralogy (Fig. 8A and B), and the petroplinthite developed on top of the Novo Remanso strata (Fig. 8C).

In addition, the He-U-Th ternary diagram allows interpretation of the (i) possible mixing between different iron-oxides generations with different U-Th contents and age leading to significant age dispersion (e.g. Danišík et al., 2013; Shuster et al., 2005; Vasconcelos et al., 2013; Monteiro et al., 2014; Heller et al., 2022), or (ii) the re-opening of goethite or hematite through different weathering phases by dissolution and He, U, Th and/or Sm loss. At the crystal scale, mixing of goethite and hematite due to hydration or dehydration or different generations of goethite and hematite can be inferred in the diagram as those minerals have different U and Th content. Secondly, the relative U and Th contents can be used as a proxy for the fractioning condition of U and Th elements during weathering processes. Indeed, aqueous fluids transported U, which can occur as a soluble compound, whereas Th is insoluble under weathering conditions (Riffel et al., 2016). Finally, the relative proportion of U and Th in each aliquot for the iron-lateritic duricrust ADC-D1 also reveals that goethite and hematite incorporate differently those elements in their crystal structure. In our samples, goethite contains relatively more Th than U, whereas hematite is richer in U compared to Th (Fig. 8).

Using the ternary diagrams, we discard data from 11 aliquots, which reveal generations mixing or re-opening events thus yielding intermediate age associated to He, U, Th and Sm contents mixing reflecting the dynamics of weathering systems (Fig. 8).

The iron-lateritic duricrust sample developed over the Alter do Chão Formation has dates ranging from 41.3 ± 4.1 to 1.1 ± 0.1 Ma, whereas the iron-lateritic duricrust sample from the profile IR-D1, developed on top of the Iranduba Formation and underlying the Novo Remanso Formation, presents (U-Th)/He ages from 28.5 ± 2.9 to 17.7 ± 1.6 Ma (Table 2; Fig. 8). Finally, the (U-Th)/He ages obtained on the iron-enrichment levels developed on top of the Novo Remanso Formation (NR-L1 & L2) (Fig. 2) range from ~3 Ma to 1 Ma (Table 2; Fig. 8).

5. Discussion

5.1. Cenozoic weathering of fluvial terraces in central Amazonia

The iron-lateritic duricrusts developed at top of the Iranduba and Alter do Chão Formations (IR-D1 and ADC-D1) imply that those fluvial deposits were in an upland position above the local erosion base level during the time of goethite and hematite precipitation. Associated with lateritic profile development, petroplinthites formation over primary sedimentary structures at top of the Novo Remanso strata (NR1 and NR2) and goethite rich levels in the Iranduba and Alter do Chão Formations (IR-L1 and ADC-L1) indicate precipitation of iron-rich levels (Figs. 2 and 3) in the non-saturated zone above the water table (e.g., Tardy, 1992). Thus, the acquisition of goethite and hematite (U-Th)/He crystallization ages on iron-enrichment levels and lateritic duricrust allows in this specific case reconstructing the time of abandonment of fluvial accumulation and the transition to long-lasting weathering conditions in central Amazonia.

Considering the (U-Th)/He data and their associate mineralogy (Fig. 9A), excluding the 11 aliquots where age mixing and U-contamination were detected, it is possible to distinguish at least two main phases of iron enrichment (iron-lateritic duricrusts and ferruginization) linked to weathering processes. The oldest weathering phase ranges from at least ~42 to ~18 Ma, with precipitation of goethite and hematite during lateritization (Figs. 2, 3 and 8A-B). This age range is defined using the (U-Th)/He data acquired in the lateritic duricrusts developed over Alter do Chão and Iranduba Formations, with the oldest age of ~42 Ma (Fig. 9; Table 2). The younger age limit at ~18 Ma was obtained in the duricrust sample developed over the Iranduba Formation (Fig. 9; Table 2). As progressive weathering can reset older weathering products through iron oxide dissolution, the (U-Th)/He ages are always minimum age. This age range between ~42 and 18 Ma obtained in duricrusts is a temporal constraint for the paleosol layers and indicates at least two weathering phases affecting the Alter do Chão and Iranduba Formations. A weathering phase older than 42 Ma is indicated by the development of the S1 lateritic paleosol on top of the Alter do Chão Formation while a second weathering phase from at least 30 to 18 Ma (Fig. 9) corresponds to the S2 lateritic paleosol developed over the Iranduba Formation (sample ADC-D1).

The ADC-D1 sample recorded older ages around ~42 (2 out of 52 ages), and ~ 30 Ma (2 out of 52 ages), with distinct U and Th contents (Fig. 5A). However, the detection of two discrete weathering events suggested by age distribution (≥42 Ma and > 30–18 Ma; Fig. 9C) is beyond the resolution of our study, as the number of dated aliquots is relatively low and the reopening of duricrusts system due to the dissolution of older hematite crystals and precipitation of younger hematite and later goethite hinder to distinguish between one single continuous phase or two discrete episodes of weathering affecting the Alter do Chão and Iranduba Formations. Nevertheless, a second weathering phase is well recorded in iron-lateritic duricrust with ages ranging from ~8 to 1 Ma, firstly with precipitation of hematite from ~8 to 3 Ma, followed by goethite precipitation from ~3 to 1 Ma (Figs. 2, 3 and 9B-C). The youngest weathering phase is mostly concomitant with the precipitation of supergene goethite associated with changes in the paleowater table position and ferruginization (Fig. 9C). Those results are in agreement with the recent study by Guinoiseau et al. (2021) on silicon isotopes in dated kaolinite present in a lateritic profile developed over Alter do Chao Formation in central Amazonia, where two main weathering episodes around 35–20 Ma and 8–6 Ma, with different weathering regimes, were identified. The first one, from ~35 to 20 Ma, represents a long

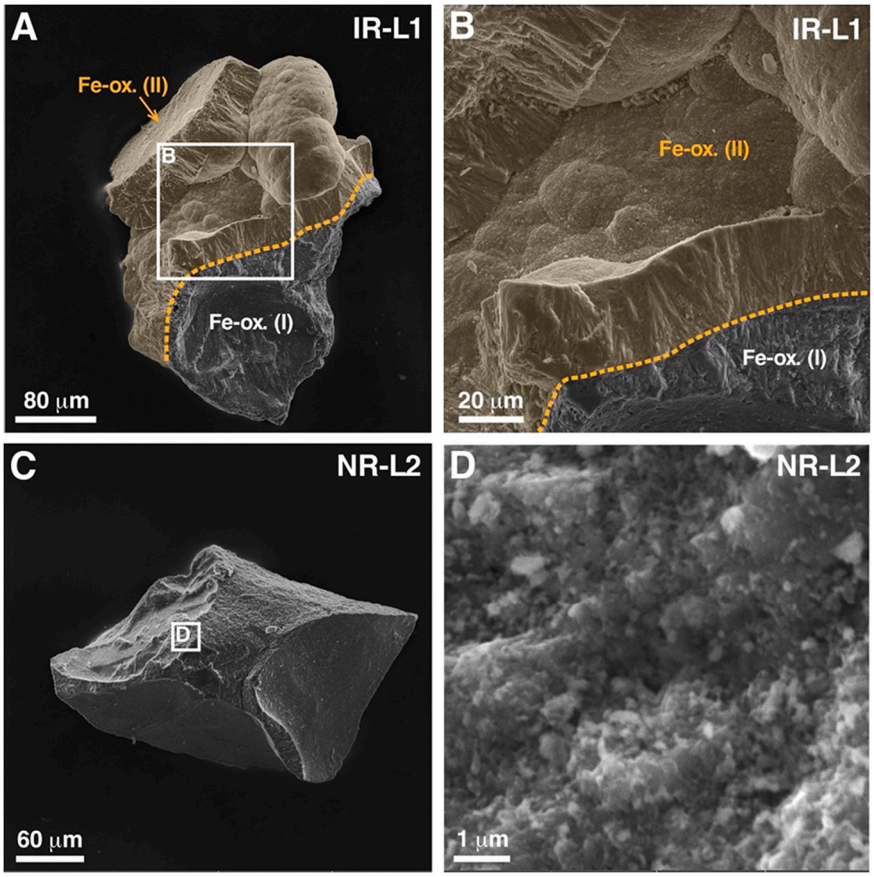

Fig. 7. Scanning electron microscopy photography of goethite fragments. Similar fragments than the one selected for (U-Th)/He dating are shown. (A) and (B) Pictures of IR-L1 sample showing the iron-oxides first generation (Fe-ox. I) and a second generation (Fe-ox. II in orange). (C) and (D) show pictures of NR-L2 sample.

episode yet with a moderate intensity, whereas the second one, from ~8 to 6 Ma, is associated with a rapid water percolation and recrystallisation of the kaolinite within the lateritic profile.

5.2. Geochronological constraints of fluvial deposits

The (U-Th)/He ages on iron-lateritic duricrust developed on top of the Alter do Chão and Iranduba Formations imply intensive and long-lasting lateritic (humid) weathering processes in central Amazonia since at least ~42 Ma. In addition, the older record of fluvial deposits exposed to lateritic weathering can be expanded to ~42–60 Ma, if the ages obtained on supergene kaolinite in the same area (Fig. 1; Balan et al., 2005) are taken into consideration. This indicates that central Amazonia is under tropical humid conditions during most of the Cenozoic. It further implies that the deposition of the upper part of Alter do Chão Formation is older than ~42 Ma (Fig. 9 A), which does not exclude a possible Paleocene age, as suggested by the biostratigraphic review presented as supplementary material. Likewise, the (U-Th)/He ages of the iron-lateritic duricrust from the Iranduba Formation yield a minimum age of ~30 Ma (Oligocene), which is older than the previously proposed Miocene age (Dino et al., 2012) (Fig. 9A). The Miocene age proposed for the Iranduba Formation was inferred based only on lithostratigraphic correlation with the Solimões Formation in western Amazonia (Dino et al., 2012). In addition, its youngest age of ~18 Ma (Fig. 9C) provides a maximum depositional age for the overlying Novo Remanso Formation, which is also supported by the biostratigraphic data (Dino et al., 2012; Guimarães et al., 2015). In addition, as the top of the Novo Remanso Formation (Fig. 2) hosts an iron-enrichment level dated at 3–1 Ma, it suggests that the upper part of the Novo Remanso Formation should be older than this age. This is in agreement with minimum ages obtained for the Novo Remanso Formation using luminescence dating methods (Bezerra et al., 2022). These results confirm the power of the (U-Th)/He geochronological method on supergene products to refine the chronostratigraphic framework of intense weathered siliciclastic sedimentary deposits ubiquitous across central Amazonia, which usually lack fossil remains for biostratigraphy.

5.3. Cenozoic landscape changes in central Amazonia

Considering that goethite precipitate during wet periods and hematite is associated with seasonal rainfall with longer dry seasons (e.g. Tardy, 1992; Zhao et al., 2017), the obtained ages of goethite and hematite could reveal a change in water availability in uplands of central Amazonia. The oldest identified weathering phase covers a period between ~42 and 18 Ma, with precipitation of goethite and hematite (Fig. 9). This weathering phase is not so well constrained in time due to the lack of primary supergene mineralogical archives, as goethite and hematite in iron-lateritic duricrust are often dissolved and recrystallized (Monteiro et al., 2014; Riffel et al., 2016; Vasconcelos et al., 2015). However, the youngest weathering phase from ~8 to 1 Ma is well-recorded in the iron-lateritic duricrust (ADC-D1) and two iron-enrichment levels developed on Alter do Chão and Iranduba Formations (ADC-L1 and IR-L1) as well as in the Novo Remanso Formation (NRL1, L2) (Figs. 2, 3 and 9). Within this time period, hematite precipitate from ~8 to 3 Ma, followed by goethite from ~3 to 1 Ma (Fig. 9). This would indicate a shift from drier to wetter climate in central Amazonia at the late Pliocene or Pleistocene.

The precipitation of iron oxides and oxyhydroxides depends on redox conditions, so when it occurs in subhorizontal layers following the land surface, the depth of its occurrence refers to the water table level (Riffel

Table 2
Iron oxides and hydroxides (U-Th)/He data.*

Sample/ Aliquot codes	Info*	^{4}He	± s	^{238}U	^{232}Th	^{147}Sm	weight	^{4}He	± s	U	Th	Sm	eU	Th/U	Raw age	± s	Corr. age	± s
		(mol)		(ng)			(μg)	(nmol/g)		(ppm)					(Ma)	(Ma)	(Ma)	(Ma)
NR-L1																		
NR-L1–1	VG	9.4E-16	9.4E-18	0.075	0.030	0.091	100	0.009	0.000	0.7	0.3	6.0	1	0.4	2.1	0.1	2.3	0.2
NR-L1–2	VG	6.2E-16	6.2E-18	0.046	0.059	0.001	81	0.008	0.000	0.6	0.7	0.1	1	1.3	1.9	0.1	2.1	0.2
NR-L1–3	VG	5.4E-16	5.4E-18	0.087	0.006	0.035	112	0.005	0.000	0.8	0.1	2.1	1	0.1	1.1	0.1	1.2	0.1
NR-L2																		
NR-L2–2	506	1.2E-15	1.2E-17	0.35	0.04	0.01	14	0.088	0.001	25.1	2.9	3.8	26	0.1	0.6	0.1	0.7	0.1
NR-L2–12	VG	1.4E-15	1.4E-17	0.217	0.048	0.011	40	0.034	0.000	5.4	1.2	1.8	6	0.2	1.1	0.1	1.2	0.1
NR-L2–13	VG	2.0E-15	2.0E-17	0.670	0.017	0.030	61	0.032	0.000	11.0	0.3	3.3	11	0.0	0.5	0.0	0.6	0.1
NR-L2–14	VG	1.7E-15	1.7E-17	1.335	0.012	0.001	42	0.039	0.000	31.8	0.3	0.2	32	0.0	0.2	0.0	0.3	0.1
NR-L2–15	907	6.9E-16	6.9E-18	0.07	0.20	0.03	71	0.010	0.000	1.0	2.8	2.4	2	2.9	1.1	0.1	1.2	0.1
NR-L2–16	908	1.4E-15	1.4E-17	0.05	0.32	0.03	87	0.016	0.000	0.6	3.6	2.4	1	6.4	2.0	0.1	2.2	0.2
NR-L2–17	909	8.9E-16	8.9E-18	0.41	0.16	0.02	61	0.015	0.000	6.6	2.6	1.8	7	0.4	0.4	0.0	0.4	0.0
NR-L2–18	910	1.2E-15	1.2E-17	0.04	0.19	0.02	61	0.019	0.000	0.7	3.1	2.1	1	4.7	2.5	0.1	2.7	0.2
NR-L2–19	911	5.3E-16	5.3E-18	0.01	0.14	0.02	23	0.023	0.000	0.6	6.2	5.0	2	10.6	2.1	0.1	2.3	0.2
NR-L2–20	913	1.8E-15	1.8E-17	0.08	0.34	0.03	52	0.036	0.000	1.6	6.5	4.0	3	4.0	2.1	0.1	2.3	0.2
IR-D																		
IR-D1–1	5470	5.1E-14	5.1E-16	0.09	1.56	0.00	33	1.546	0.015	2.7	47.3	0.0	15	17.5	20.7	2.1	22.8	2.3
IR-D1-A	5918	4.5E-14	4.5E-16	0.08	1.39	0.01	29	1.546	0.015	2.7	48.0	1.3	15	18.1	20.5	2.0	22.5	2.3
IR-D1-B	5919	3.7E-14	3.7E-16	0.09	0.89	0.07	40	0.920	0.009	2.3	22.3	11.8	8	9.5	22.4	2.2	24.6	2.5
IR-D1-C	5922	8.7E-14	8.7E-16	0.14	2.23	0.00	46	1.899	0.019	3.0	48.4	0.0	15	16.0	24.3	2.4	26.8	2.7
IR-D1-F	5925	4.2E-14	4.2E-16	0.07	1.28	0.00	25	1.680	0.017	2.9	51.3	0.5	16	17.8	20.8	2.1	22.8	2.3
IR-D1–1	457	2.3E-13	2.3E-15	0.24	6.65	0.00	118	1.970	0.020	2.1	56.4	0.1	16	27.3	23.7	1.9	26.1	2.4
IR-D1–3	459	2.3E-14	2.3E-16	0.02	1.06	0.00	33	0.701	0.007	0.5	32.2	0.1	9	69.5	16.1	1.3	17.7	1.6
IR-D1–4	460	1.3E-13	1.3E-15	0.15	3.85	0.00	58	2.230	0.022	2.5	66.4	0.1	19	26.6	22.7	1.8	25.0	2.3
IR-D1–6	462	3.9E-14	3.9E-16	0.06	1.38	0.00	30	1.298	0.013	2.1	46.1	0.1	14	21.5	18.4	1.5	20.3	1.8
IR-D1–7	464	2.3E-13	2.3E-15	0.23	6.12	0.00	125	1.867	0.019	1.8	49.0	0.1	14	27.2	25.9	2.1	28.5	2.6
IR-D1–8	467	1.3E-13	1.3E-15	0.13	4.85	0.00	86	1.524	0.015	1.5	56.3	0.1	16	37.7	19.1	1.5	21.0	1.9
IR-D1–9	468	1.0E-13	1.0E-15	0.66	3.59	0.01	41	2.512	0.025	16.2	87.5	1.0	38	5.4	12.6	1.0	13.9	1.3
IR-D1–10	469	5.4E-14	5.4E-16	0.04	2.08	0.00	55	0.984	0.010	0.7	37.8	0.4	10	55.9	19.0	1.5	20.9	1.9
IR-D1–11	470	6.6E-13	6.6E-15	1.65	21.25	0.01	169	3.915	0.039	9.8	125.8	0.3	41	12.9	18.4	1.5	20.2	1.8
IR-D1–12	471	4.4E-13	4.4E-15	0.98	13.77	0.00	174	2.512	0.025	5.6	79.1	0.2	25	14.1	19.2	1.5	21.1	1.9
IR-L1																		
IR-L1–2	482	1.2E-14	1.2E-16	0.09	0.08	0.01	20	0.591	0.006	4.7	4.0	1.8	6	0.9	19.4	1.6	21.4	1.9
IR-L1–4	484	3.7E-15	3.7E-17	0.10	0.25	0.00	44	0.084	0.001	2.4	5.8	0.5	4	2.4	4.2	0.3	4.6	0.4
IR-L1–13	512	1.6E-15	1.6E-17	0.12	0.23	0.00	33	0.050	0.000	3.7	7.1	0.2	5	1.9	1.7	0.1	1.9	0.2
IR-L1–14	VG	3.6E-15	3.6E-17	0.160	0.175	0.000	91	0.039	0.000	1.8	1.9	0.0	2	1.1	3.3	0.2	3.6	0.4
IR-L1–15	VG	6.4E-15	6.4E-17	0.180	0.125	0.000	112	0.057	0.001	1.6	1.1	0.0	2	0.7	5.6	0.3	6.2	0.6
IR-L1–16	VG	1.2E-14	1.2E-16	0.132	0.160	0.000	80	0.144	0.001	1.6	2.0	0.0	2	1.2	12.6	0.8	13.9	1.4
IR-L1–17	VG	4.0E-15	4.0E-17	0.196	0.240	0.685	109	0.036	0.000	1.8	2.2	41.9	2	1.2	2.8	0.2	3.1	0.3
IR-L1–18	962	4.8E-15	4.8E-17	0.16	0.39	0.00	58	0.082	0.001	2.7	6.8	0.3	4	2.5	3.5	0.3	3.9	0.4
IR-L1–19	964	1.5E-14	1.5E-16	0.21	0.30	0.00	73	0.211	0.002	2.8	4.1	0.2	4	1.4	10.2	0.8	11.3	1.1
IR-L1–20	917	5.4E-15	5.4E-17	0.12	0.63	0.00	98	0.055	0.001	1.3	6.4	0.2	3	5.1	3.7	0.3	4.1	0.4
IR-L1–21	919	5.0E-15	5.0E-17	0.11	0.40	0.00	89	0.056	0.001	1.3	4.5	0.2	2	3.5	4.4	0.4	4.8	0.5
IR-L1–22	920	3.4E-15	3.4E-17	0.21	0.38	0.00	79	0.043	0.000	2.7	4.8	0.2	4	1.7	2.1	0.2	2.3	0.2
IR-L1–23	921	3.9E-15	3.9E-17	0.25	0.34	0.00	74	0.053	0.001	3.4	4.6	0.2	5	1.3	2.2	0.2	2.4	0.2
IR-L1–24	922	6.5E-15	6.5E-17	0.18	0.38	0.00	72	0.090	0.001	2.4	5.3	0.3	4	2.2	4.5	0.4	5.0	0.5
IR-L1–25	923	7.4E-15	7.4E-17	0.35	0.70	0.00	120	0.062	0.001	2.9	5.8	0.2	4	2.0	2.7	0.2	2.9	0.3

(*continued on next page*)

Table 2 (*continued*)

Sample/ Aliquot codes	Info*	^{4}He	± s	^{238}U	^{232}Th	^{147}Sm	weight	^{4}He	± s	U	Th	Sm	eU	Th/U	Raw age	± s	Corr. age	± s
		(mol)		(ng)			(µg)	(nmol/g)		(ppm)					(Ma)	(Ma)	(Ma)	(Ma)
IR-L1–26	924	1.9E-14	1.9E-16	0.16	0.45	0.00	94	0.205	0.002	1.7	4.8	0.2	3	2.8	13.4	1.1	14.7	1.5
IR-L1–27	927	4.7E-14	4.7E-16	0.38	0.95	0.01	112	0.416	0.004	3.4	8.5	0.3	5	2.5	14.2	1.1	15.6	1.6
ADC-L1																		
ADC-L1–1B	540	4.1E-15	4.1E-17	0.12	0.03	0.04	32	0.130	0.001	3.8	0.9	7.7	8	0.2	6.0	0.5	6.6	0.6
ADC-L1–1C	541	6.5E-15	6.5E-17	0.30	0.03	0.05	42	0.156	0.002	7.1	0.8	8.4	8	0.1	4.0	0.3	4.4	0.4
ADC-L1–1D	542	7.2E-15	7.2E-17	0.35	0.03	0.04	54	0.133	0.001	6.6	0.6	5.2	5	0.1	3.7	0.3	4.1	0.4
ADC-L1–2A	543	5.8E-15	5.8E-17	0.35	0.05	0.04	29	0.199	0.002	12.2	1.6	8.2	8	0.1	2.9	0.2	3.2	0.3
ADC-L1–2B	544	2.7E-15	2.7E-17	0.21	0.05	0.01	13	0.204	0.002	15.8	4.0	4.5	5	0.3	2.3	0.2	2.5	0.2
ADC-L1–2C	545	2.4E-15	2.4E-17	0.13	0.04	0.02	19	0.127	0.001	6.9	2.3	6.1	6	0.3	3.2	0.3	3.5	0.3
ADC-L1–3A	549	9.1E-15	9.1E-17	0.49	0.05	0.05	33	0.275	0.003	14.7	1.6	10.4	10	0.1	3.4	0.3	3.7	0.3
ADC-L1–3B	546	5.8E-15	5.8E-17	0.46	0.08	0.03	36	0.161	0.002	12.9	2.3	5.4	5	0.2	2.2	0.2	2.4	0.2
ADC-L1–15	929	1.3E-14	1.3E-16	0.39	0.06	0.11	51	0.252	0.003	7.7	1.2	14.0	8	0.2	5.9	0.5	6.5	0.6
ADC-L1–31	930	1.4E-14	1.4E-16	0.85	0.24	0.05	45	0.320	0.003	18.9	5.4	7.7	20	0.3	2.9	0.2	3.2	0.3
ADC-L1–11	931	1.6E-14	1.6E-16	0.46	0.05	0.10	112	0.140	0.001	4.1	0.4	6.2	4	0.1	6.1	0.5	6.7	0.7
ADC-L1–12	932	1.2E-14	1.2E-16	0.44	0.04	0.07	55	0.217	0.002	8.1	0.8	8.8	8	0.1	4.9	0.4	5.3	0.5
ADC-L1–13	933	1.6E-14	1.6E-16	0.39	0.06	0.13	104	0.151	0.002	3.8	0.6	8.4	4	0.2	7.2	0.6	7.9	0.8
ADC-L1–32	936	1.3E-14	1.3E-16	0.80	0.08	0.07	57	0.222	0.002	14.0	1.3	8.0	14	0.1	2.9	0.2	3.1	0.3
ADC-L1–33	937	1.8E-14	1.8E-16	1.19	0.21	0.08	67	0.263	0.003	17.8	3.2	7.9	19	0.2	2.6	0.2	2.9	0.3
ADC-L1–34	938	1.4E-14	1.4E-16	0.84	0.08	0.06	70	0.204	0.002	11.9	1.1	6.0	12	0.1	3.1	0.2	3.4	0.3
ADC-L1–35	940	2.7E-14	2.7E-16	1.59	0.49	0.10	92	0.289	0.003	17.2	5.3	7.3	19	0.3	2.9	0.2	3.2	0.3
ADC-D1																		
ADC-D1#1																		
Hematite																		
ADC-D1#1-AH1	983	3.2E-15	3.2E-17	0.13	0.10	0.01	37	0.085	0.001	3.4	2.7	1.4	4	0.8	4.0	0.3	4.4	0.4
ADC-D1#1-AH2	984	1.1E-14	1.1E-16	0.44	0.49	0.02	67	0.158	0.002	6.5	7.3	1.9	8	1.1	3.6	0.3	3.9	0.4
ADC-D1#1-AH3	985	1.1E-14	1.1E-16	0.44	0.23	0.02	56	0.199	0.002	7.7	4.0	2.3	9	0.5	4.3	0.3	4.7	0.5
ADC-D1#1-AH4	986	8.7E-15	8.7E-17	0.37	0.29	0.01	52	0.166	0.002	7.0	5.5	1.9	8	0.8	3.7	0.3	4.1	0.4
ADC-D1#1-AH5	988	1.2E-14	1.2E-16	0.36	0.22	0.03	39	0.307	0.003	9.2	5.5	5.3	10	0.6	5.4	0.4	6.0	0.6
Hematite												0.0						
ADC-D1#1-BH1	989	2.5E-14	2.5E-16	0.85	0.39	0.05	49	0.498	0.005	17.3	7.9	7.0	19	0.5	4.8	0.4	5.3	0.5
ADC-D1#1-BH2	991	2.2E-15	2.2E-17	0.09	0.08	0.00	36	0.062	0.001	2.6	2.1	0.9	3	0.8	3.7	0.3	4.1	0.4
ADC-D1#1-BH 3	992	5.3E-15	5.3E-17	0.19	0.17	0.01	30	0.174	0.002	6.2	5.7	2.8	8	0.9	4.3	0.3	4.7	0.5
ADC-D1#1-BH4	993	1.0E-14	1.0E-16	0.45	0.23	0.03	58	0.178	0.002	7.8	3.9	3.2	9	0.5	3.8	0.3	4.2	0.4
ADC-D1#1-BH 5	994	2.0E-14	2.0E-16	0.82	0.40	0.04	76	0.265	0.003	10.7	5.2	3.1	12	0.5	4.1	0.3	4.5	0.5
Goethite																		
ADC-D1#1-GA1	996	3.3E-14	3.3E-16	0.29	1.01	0.05	43	0.770	0.008	6.8	23.3	8.3	12	3.4	11.7	0.9	12.8	1.3
ADC-D1#1-GA2	997	3.1E-15	3.1E-17	0.15	0.85	0.02	35	0.087	0.001	4.3	23.9	4.6	10	5.6	1.6	0.1	1.8	0.2
ADC-D1#1-GA3	998	1.9E-15	1.9E-17	0.14	0.49	0.02	71	0.026	0.000	1.9	6.9	2.1	4	3.6	1.4	0.1	1.5	0.2
ADC-D1#1-GA4	999	3.3E-15	3.3E-17	0.27	1.28	0.04	35	0.093	0.001	7.6	36.2	7.0	16	4.8	1.1	0.1	1.2	0.1
ADC-D1#1-GA5	1000	4.6E-15	4.6E-17	0.15	0.75	0.03	51	0.089	0.001	2.9	14.6	3.5	6	5.0	2.6	0.2	2.8	0.3
Goethite																		
ADC-D1#1-GB1	1064	1.2E-14	1.2E-16	0.55	1.69	0.08	60	0.199	0.002	9.1	27.9	8.6	16	3.1	2.4	0.2	2.6	0.3
ADC-D2#2																		
Hematite																		
ADC-D1#2-HB1	941	8.9E-15	8.9E-17	0.25	0.12	0.02	15	0.576	0.006	16.5	7.8	7.5	18	0.5	5.8	0.5	6.4	0.6
ADC-D1#2-HB2	942	5.9E-14	5.9E-16	0.38	0.13	0.02	90	0.656	0.007	4.2	1.4	1.2	5	0.3	26.7	2.1	29.4	2.9
ADC-D1#2-HB4	946	4.6E-14	4.6E-16	0.21	0.10	0.01	45	1.022	0.010	4.6	2.2	1.3	5	0.5	36.7	2.9	40.4	4.0
ADC-D1#2-HB5	947	7.7E-15	7.7E-17	0.31	0.15	0.02	42	0.181	0.002	7.4	3.6	3.5	8	0.5	4.1	0.3	4.5	0.4
ADC-D1#2-HB6	2216	1.8E-14	1.6E-16	0.82	0.41	0.06	68	0.263	0.002	12.1	6.0	5.8	14	0.5	3.6	0.1	4.0	0.4

(*continued on next page*)

Table 2 (*continued*)

Sample/ Aliquot codes	Info*	^{4}He	± s	^{238}U	^{232}Th	^{147}Sm	weight	^{4}He	± s	U	Th	Sm	eU	Th/U	Raw age	± s	Corr. age	± s
		(mol)		(ng)			(μg)	(nmol/g)		(ppm)					(Ma)	(Ma)	(Ma)	(Ma)
ADC-D1#2-HB7	2217	3.2E-14	2.2E-16	1.12	0.57	0.08	99	0.322	0.002	11.3	5.7	5.3	13	0.5	4.7	0.2	5.2	0.5
ADC-D1#2-HB8	2218	8.8E-15	1.0E-16	0.58	0.32	0.03	58	0.152	0.002	10.1	5.6	3.2	11	0.6	2.5	0.1	2.7	0.3
ADC-D1#2-HB9	2219	1.4E-14	1.7E-16	0.65	0.30	0.05	65	0.216	0.003	10.0	4.6	4.8	11	0.5	3.6	0.2	4.0	0.4
ADC-D1#2-HB10	2222	1.1E-14	1.7E-16	0.58	0.35	0.03	50	0.225	0.003	11.6	7.1	4.4	13	0.6	3.1	0.1	3.5	0.3
ADC-D1#2-HB11	2224	1.2E-14	8.3E-17	0.61	0.27	0.03	50	0.234	0.002	12.2	5.4	4.4	14	0.4	3.2	0.1	3.5	0.4
ADC-D1#2-HB12	2226	1.1E-14	1.2E-16	0.45	0.31	0.03	65	0.163	0.002	7.0	4.8	3.5	8	0.7	3.7	0.2	4.1	0.4
ADC-D1#2-HB13	2227	3.0E-14	1.7E-16	1.58	0.62	0.07	130	0.232	0.001	12.2	4.8	3.6	13	0.4	3.2	0.1	3.6	0.4
ADC-D1#2-HB14	2228	1.9E-14	1.4E-16	0.68	0.52	0.06	64	0.298	0.002	10.6	8.1	6.0	13	0.8	4.4	0.2	4.8	0.5
Hematite																		
ADC-D1#2-HA1	969	2.4E-14	2.4E-16	1.07	0.57	0.05	87	0.277	0.003	12.3	6.6	3.9	14	0.5	3.7	0.3	4.1	0.4
ADC-D1#2-HA2	971	1.1E-14	1.1E-16	0.54	0.31	0.03	111	0.103	0.001	4.8	2.8	1.8	6	0.6	3.5	0.3	3.8	0.4
ADC-D1#2-HA3	972	1.2E-14	1.2E-16	0.16	0.65	0.03	44	0.276	0.003	3.6	14.5	4.3	7	4.0	7.2	0.6	8.0	0.8
ADC-D1#2-HA4	974	1.3E-13	1.3E-15	0.49	0.61	0.04	45	2.833	0.028	10.8	13.4	5.2	14	1.2	37.6	3.0	41.3	4.1
ADC-D1#2-HA5	975	3.0E-15	3.0E-17	0.14	0.30	0.02	31	0.096	0.001	4.6	9.6	3.4	7	2.1	2.6	0.2	2.9	0.3
ADC-D1#2-HA6	2201	2.2E-14	2.2E-16	1.13	0.57	0.06	96	0.226	0.002	11.8	6.0	4.3	13	0.5	3.2	0.1	3.5	0.3
ADC-D1#2-HA7	2203	1.4E-14	1.2E-16	0.50	0.24	0.05	58	0.237	0.002	8.6	4.1	6.0	10	0.5	4.6	0.2	5.1	0.5
ADC-D1#2-HA8	2204	3.2E-14	1.9E-16	1.55	0.71	0.09	107	0.298	0.002	14.5	6.7	5.4	16	0.5	3.4	0.1	3.8	0.4
ADC-D1#2-HA9	2205	1.4E-14	1.0E-16	0.65	0.32	0.05	55	0.252	0.002	11.9	5.8	5.9	13	0.5	3.5	0.1	3.9	0.4
ADC-D1#2-HA10	2207	1.5E-14	1.1E-16	0.71	0.56	0.09	94	0.162	0.001	7.6	6.0	6.7	9	0.8	3.3	0.1	3.7	0.4
ADC-D1#2-HA11	2208	3.2E-14	2.4E-16	1.13	0.48	0.10	114	0.284	0.002	9.9	4.2	5.7	11	0.4	4.8	0.2	5.3	0.5
ADC-D1#2-HA12	2209	3.0E-14	3.2E-16	1.35	0.61	0.11	107	0.278	0.003	12.6	5.7	6.6	14	0.5	3.7	0.1	4.0	0.4
ADC-D1#2-HA13	2210	1.8E-14	1.6E-16	0.89	1.07	0.04	79	0.226	0.002	11.3	13.5	3.0	15	1.2	2.9	0.1	3.2	0.3
ADC-D1#2-HA14	2211	8.2E-14	5.6E-16	0.53	0.28	0.04	72	1.139	0.008	7.4	3.8	3.3	8	0.5	25.5	0.9	28.0	2.8
Goethite cortex																		
ADC-D1#2-GA1	948	4.7E-15	4.7E-17	0.14	0.96	0.02	28	0.167	0.002	5.0	33.7	5.7	13	6.8	2.4	0.2	2.6	0.3
ADC-D1#2-GA2	951	5.5E-15	5.5E-17	0.12	1.03	0.02	27	0.202	0.002	4.3	37.4	5.0	13	8.8	2.9	0.2	3.1	0.3
ADC-D1#2-GA3	952	2.6E-15	2.6E-17	0.24	0.96	0.05	56	0.046	0.000	4.2	17.1	6.0	8	4.0	1.0	0.1	1.1	0.1
ADC-D1#2-GA4	955	5.4E-15	5.4E-17	0.34	2.05	0.05	68	0.079	0.001	5.0	30.0	4.8	12	6.0	1.2	0.1	1.3	0.1
Goethite cortex																		
ADC-D1#2-GB1	976	7.6E-15	7.6E-17	0.26	1.41	0.04	91	0.083	0.001	2.8	15.4	3.2	7	5.5	2.4	0.2	2.6	0.3
ADC-D1#2-GB2	977	2.2E-15	2.2E-17	0.06	0.37	0.01	21	0.101	0.001	3.0	17.3	3.5	7	5.8	2.7	0.2	2.9	0.3
ADC-D1#2-GB3	978	3.0E-15	3.0E-17	0.08	0.54	0.01	24	0.121	0.001	3.5	22.1	3.2	9	6.4	2.6	0.2	2.8	0.3
ADC-D1#2-GB4	980	6.7E-15	6.7E-17	0.17	0.86	0.03	56	0.120	0.001	3.1	15.3	3.8	7	5.0	3.3	0.3	3.6	0.4
ADC-D12#2-GB5	981	1.5E-14	1.5E-16	0.29	1.30	0.05	48	0.318	0.003	6.0	26.8	7.5	12	4.5	4.8	0.4	5.2	0.5

Effective Uranium content eU = [U] + 0.238 × [Th] + 0.0012 × [Sm] in ppm.

* Information about the analysis. Aliquots analyzed with the He extraction line coupled with a quadrupole are marked with their pipette number and analysis has been performed in September 2018 (pipette ranging from 5470 and 5925, and from March to August 2019 for pipette number ranging from 457 to 940). Aliquots analyzed with the He extraction line coupled to a VG5400 mass spectrometer in April 2019 are identified with VG name.

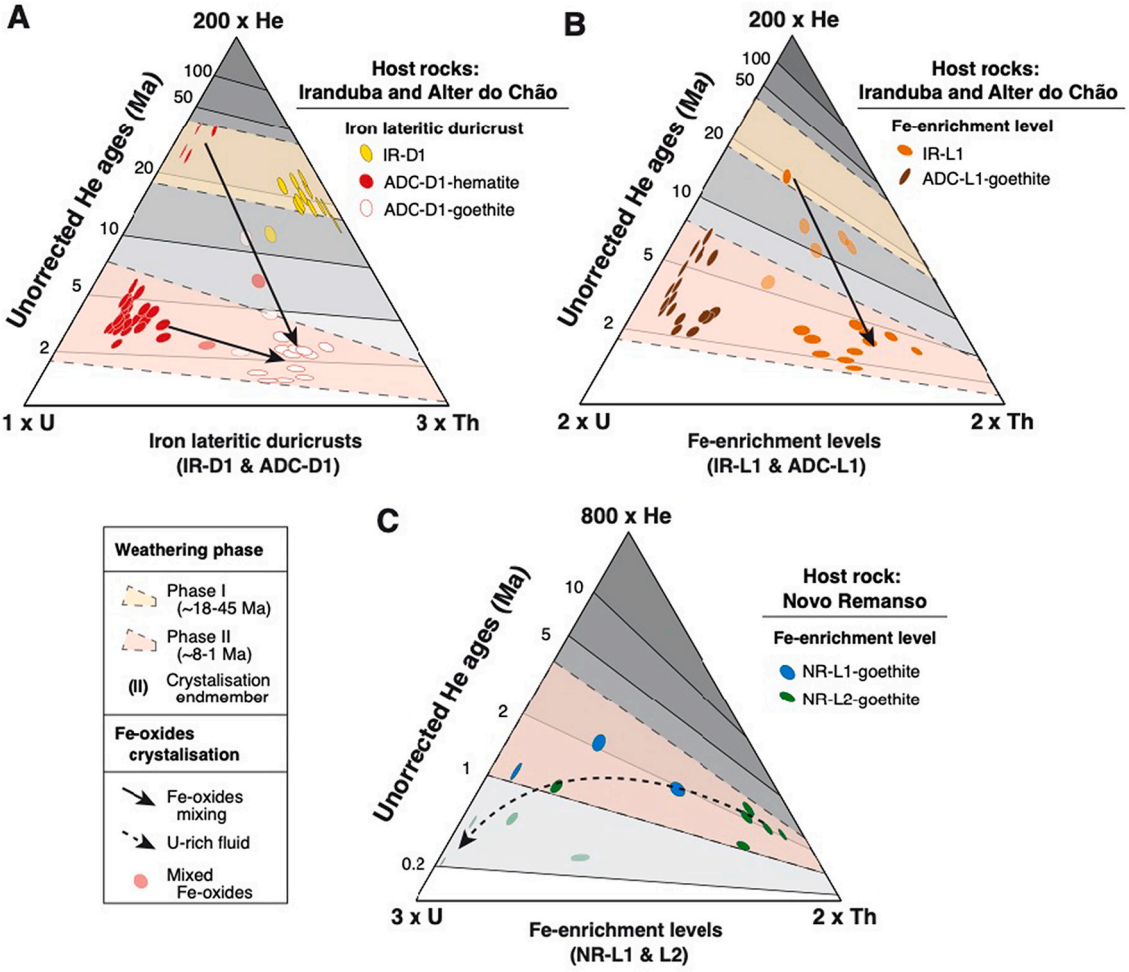

Fig. 8. Evolution of the (U-Th)/He ages on a He-U-Th ternary diagram. (A) He-U-Th ternary diagram of the iron-lateritic duricrust (ADC-D1 hematite and goethite generations and IR-D1) samples. (B) He-U-Th ternary diagram of the iron-enrichment levels (ADC-L1 and IR-L1) developed on Alter do Chão. (C) He-U-Th ternary diagram of the iron-enrichment levels (NR-L1 and NR-L2) developed on Novo Remanso Formation. The main identified phases of weathering are indicated, in addition to the crystallization end-members. The ternary diagrams allow to highlight the effects of iron-oxides mixing and U-rich fluid contamination in the distribution of parent and radiogenic elements. Ternary diagram among He, U and Th contents is build using the HelioPlot program (Vermeesch, 2010).

et al., 2016). The samples with ages of ~8–1 Ma can indicate that the past water table was at a higher position (Fig. 9) in relation to the modern water table. This implies that the deposition of the upper part of the Novo Remanso Formation should be older than 8 Ma (Fig. 9C), which supports the Miocene age inferred through biostratigraphy (Dino et al., 2012; Guimarães et al., 2015). Finally, iron-enrichment levels (i.e., petroplinthites) developed on the uppermost part of the Novo Remanso Formation yielded ages from ~3 to 1 Ma, indicating that the Novo Remanso fluvial deposits were abandoned and exposed to weathering since at least that time, i.e., in the late Pliocene (Guimarães et al., 2015; Soares et al., 2015) (Fig. 6) or Pleistocene. Alluvial plains along the large rivers draining central Amazonia may have retreated during the late Pliocene or Pleistocene (<3 Ma) due to channel incision (Bezerra et al., 2022). The crystallization of a secondary goethite phase on the hematite-rich iron-lateritic duricrust sample from ~3 to 1 Ma suggests a major change to a more humid climate (Figs. 6 and 9). The supergene phases reported in this study suggest that ancient fluvial deposits forming ancient alluvial plains were converted into stable uplands in central Amazonia during the Cenozoic, where the youngest recorded phase of upland expansion ranges from the late Miocene to late Pliocene/Pleistocene. This younger phase of upland expansion over fluvial deposits is also recorded by Electron Paramagnetic Resonance (EPR) ages in kaolinite obtained by Balan et al. (2005) and silicon isotopes obtained on the same samples by Guinoiseau et al. (2021) in lateritic profiles of the Alter do Chão Formation as well as by luminescence ages in undifferentiated deposits overlaying the Novo Remanso Formation in central and eastern Amazonia (Bezerra et al., 2022) and EPR ages in kaolinite and (U-Th)/He ages in goethite from the Içá Formation in northwestern Amazonia (Allard et al., 2018; Allard et al., 2020) farther upstream on the Negro River (Fig. 1). All those geochronological data allow us to improve the age limits of the chronostratigraphic framework for central Amazonia as shown in Fig. 9A.

The global progressive cooling since ~50 Ma, with intensification since 5 Ma (Westerhold et al., 2020) and rising of closed-canopy rainforests since the Paleogene (Carvalho et al., 2021) could change precipitation patterns across lowland Amazonia and occasionally enhanced lateritic weathering processes. Global colling could enhance sea surface temperature gradients between tropical and extratropical regions and increase the inland transport of moisture from the equatorial Atlantic (Bertassoli Jr et al., 2019) while denser rainforests contribute to continental water recycling and higher precipitation as demonstrated by model simulations (e.g., Nobre et al., 1991). Macrofossil and palynology-based reconstructions of paleoelevation in the northernmost Central Andean Plateau document a kilometer-scale surface uplift between ~9 and 5 Ma and drier Pliocene in the Andean hinterland (Martínez et al., 2020), which may have trigger a wetter climate in western Amazon associated with orographic precipitation since the Pliocene. Similar uplift patterns are documented in the northernmost Amazonian

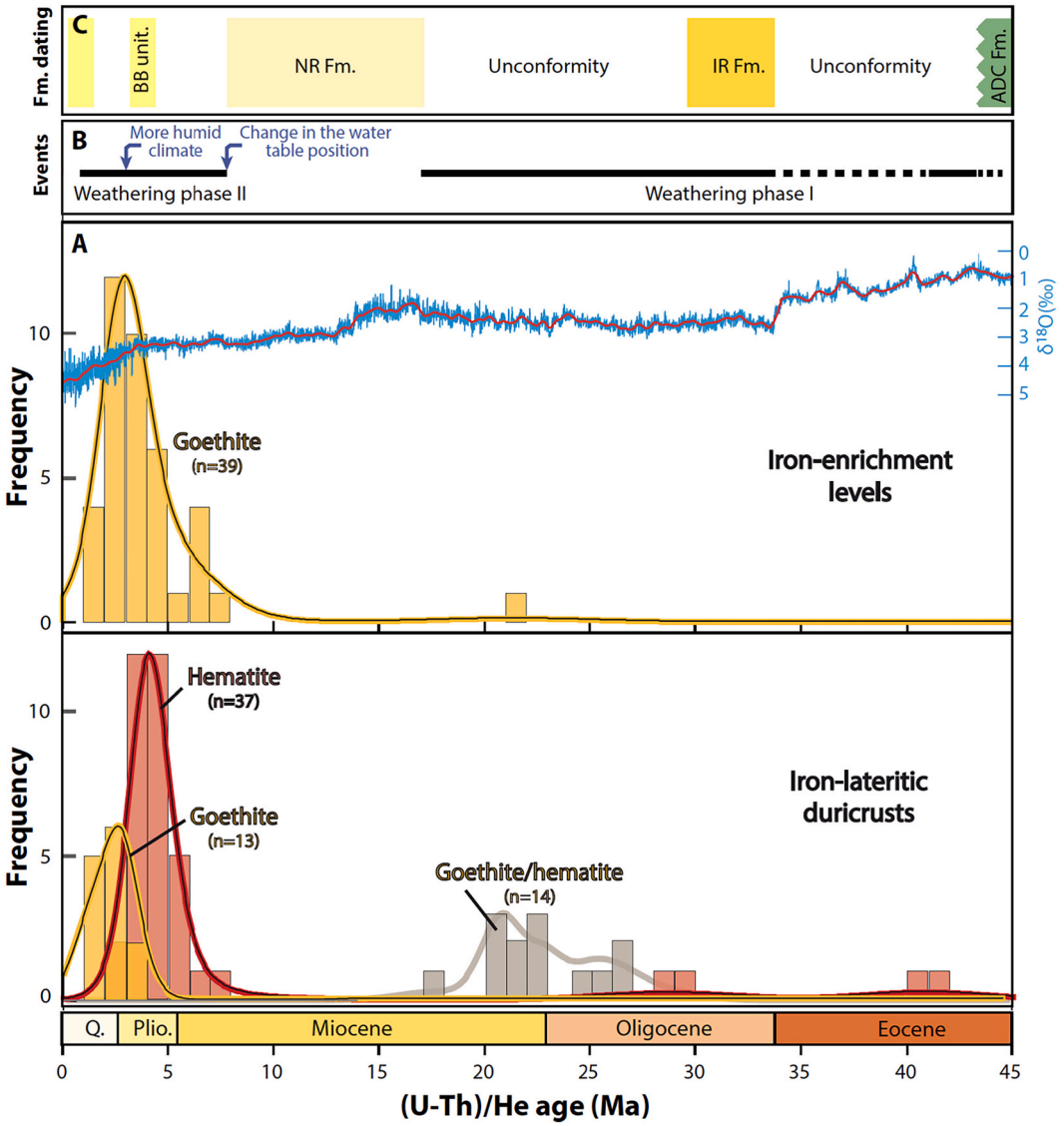

Fig. 9. Distribution of (U-Th)/He ages for samples from this study. (A) and (B) Interpreted age information and weathering phases recorded in the Alter do Chão, Iranduba, and Novo Remanso Formations. The Barro Branco (BB) unit and undifferentiated Quaternary sediments are also represented. (C) Age histograms and probability curves obtained on iron-duricrusts and iron-enrichment levels developed on the Alter do Chão (ADC) and Iranduba (IR) Formations and Fe-enrichment levels developed on the Novo Remanso (NR) Formation. Mineralogical data and the global $\delta^{18}O$ curve from benthic foraminifer are presented for comparison (Westerhold et al., 2020). For the iron-duricrust sample developed on the Iranduba Formation, minerals were not discriminated and can be goethite or hematite.

Andes in southern Colombia between 6 and 3 Ma (Anderson et al., 2016; Mora et al., 2008). For example, massive gravel progradation since the late Miocene-Pliocene in the Llanos Basin of Colombia agrees with main Andean erosion (Parra et al., 2010), a wetter climate, and higher relief. In addition, the global sea-level fall and increase of climate variability during the Pleistocene (Zachos et al., 2001; Westerhold et al., 2020) may also have prompted the rise of stream power in Andean tributaries, leading to erosion through the watershed, incision in the main lowland rivers (Pupim et al., 2019) and an increase of sedimentation rate offshore the Amazon River mouth (Hoorn et al., 2017). In this case, rivers draining central Amazonia should be connected with the Andes during the late Miocene and Pliocene (e.g., Figueiredo et al., 2009), implying the presence of a transcontinental Amazon River. However, sediment provenance data would be necessary to evaluate if the former transcontinental river is equivalent to the modern course of the Amazon River.

Integrating data from this study and from the literature, we proposed a paleogeographic reconstitution for central Amazonia since the Eocene, which describes changes in the fluvial landscape and assembly of biogeographic boundaries for upland species (Fig. 10).

The iron-lateritic duricrusts ages indicate that the Alter do Chão Formation was an abandoned alluvial plain (i.e., fluvial terraces) at least from 42 Ma (Figs. 9A-B). Associated with the development of lateritic profiles, an upland tropical rainforest should already be established at ~42 Ma on the outcrop belt of the Alter do Chão Formation (Figs. 1 and 10A). After 30 Ma, the Iranduba Formation was deposited locally from a northwestern cratonic sediment source, and undergone weathering until ~18 Ma (Figs. 10A-B-C). Our data unfortunately do not allow distinguishing between a continuous weathering phase from ~42 to 18 Ma or two discrete weathering phases (~42 Ma and 30–18 Ma). However, the obtained ages indicate that the deposition of the Novo Remanso Formation on top of the Iranduba Formation occurred after 18 Ma, associated with eastward sediment passing though. This is interpreted as a new phase of sediment accumulation and expansion of floodplains under a higher base level (Fig. 10D). From ~8 Ma, a second weathering phase is recorded in the Alter do Chão Formations, with wetter climatic

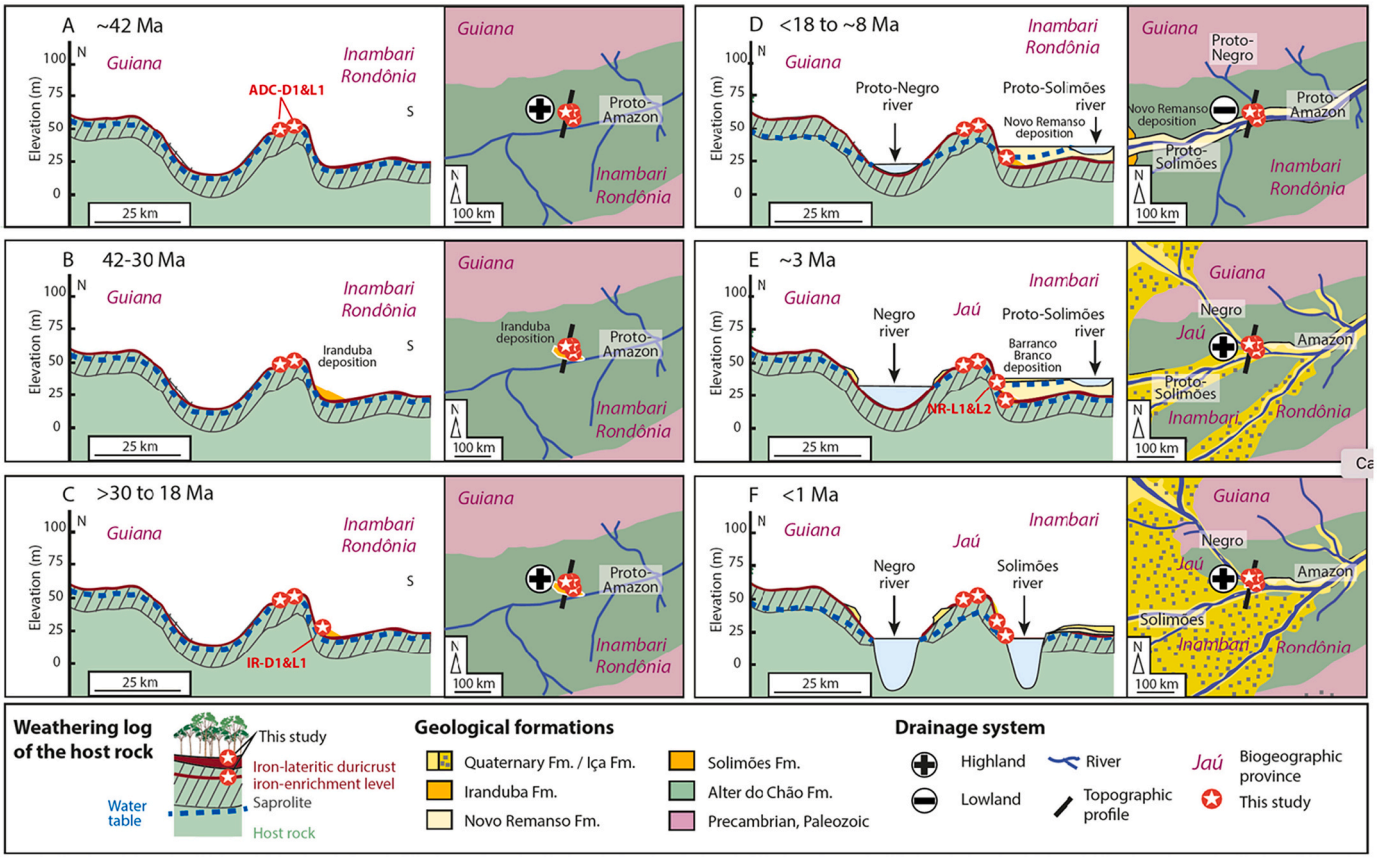

Fig. 10. Reconstitution of central Amazonia upland paleobiogeographic boundaries and associated weathering. (A) ~42 Ma: expanded upland under lower base level and associated lateritic weathering of fluvial terraces. This phase corresponds to the alluvial plains of the Alter do Chão Formation and further abandonment and weathering due to base level fall. The direction of flow of the paleo-amazon river is noted, even if it is unconstrained. (B) 42–30 Ma: Local accumulation of the Iranduba Formation under higher base level, with sediments from cratonic northwestern sources. (C) >30 to 18 Ma: expanded upland under lower base level and associated lateritic weathering of fluvial terraces represented by the Iranduba Formation (D) <18 to ~8 Ma: new phase of expansion of floodplains and fluvial sedimentation under higher base level allowing the accumulation of the Novo Remanso Formation, from a western source. (E) ~3 Ma: alluvial plain retreat under lower base level, highlighting the last massive weathering event of the Novo Remanso deposits. (F) < 1 Ma: full development of the Negro and Solimões rivers with channel incision associated with lower base level. The boundaries of the Guiana, Jaú, Inambari and Rondônia biogeographic provinces were defined according to Ribas et al. (2012). For simplification, the vegetation of alluvial and upland terrains has been removed from the landscape reconstruction sketches.

conditions at 3 Ma, which would be associated with new expansion of uplands and the downcutting of the lower Negro River valley (Fig. 10E). The weathering phase at 8–6 Ma is also recoded within the kaolinite from the lateritic profile of the Alter do Chão Formation in central Amazonia (Guinoiseau et al., 2021). Finally, authigenic iron products younger than 1 Ma are absent in the iron-lateritic duricrust and iron-enrichment level, implying a shift in lateritic weathering conditions during the Pleistocene, possibly because soil profiles reached a steady-state condition due to progressive river incision and falling water table in central Amazonia (Fig. 10F). Despite the studied fluvial deposits and their supergene iron-oxide products record major episodes of sediment accumulation (alluvial plain expansion) and weathering (upland expansion) in a time span of millions of years, both processes could occur in smaller timespans. The study area differs from westward areas in lowland Amazonia, where higher sediment accommodation space allows the preservation of series of fluvial terraces recording Pleistocene aggradation and incision phases (Pupim et al., 2019). On the other hand, fluvial valleys in central and eastern Amazonia are more incised and bounded by Cretaceous sedimentary rocks with higher resistance to erosion, which reduce sediment accumulation space and favor recycling of ancient fluvial deposits hosting paleosols (Bezerra et al., 2022).

5.4. *Implications for central Amazonia biogeography*

The past riverine landscapes of central Amazonia during the Cenozoic have direct implications for the environments sustaining specific animal and plant species (Cracraft et al., 2020). Our geochronological data provides a minimum age of ~3 Ma for the down-cutting of the Negro River into a large valley to become the second largest tributary of the Amazon River and rearrange major biogeographic boundaries in central Amazonia. Currently, important ecological differences exist between non-flooded areas with closed canopy upland forests (Terra Firme) and seasonally inundated floodplain forests (Várzea and Igapó) along the large Amazonian rivers (Junk et al., 2011). Specific species occur at these distinct habitats and the transitions from alluvial plains with seasonally flooded ecosystems to upland forests evidenced here would have affected species distributions and connectivity among populations, as well as the assemblage of local biological communities (Crouch et al., 2018).

The Eocene-Miocene weathering phase (~42–18 Ma) on fluvial deposits of Alter do Chão Formation suggests the conversion of paleo-floodplains into long-lasting upland environments across central Amazonia. During this time, upland forests north of the Amazon River in central Amazonia were probably continuous, and the Guiana and Jaú biogeographic provinces should have formed a continuous emerged area (Fig. 10A) drained by small rivers. By 30 Ma, a phase of floodplains

expansion had developed locally with the deposition of the Iranduba Formation from a northwestern drainage (Fig. 10B). Weathering of fluvial terraces from 30 to 18 Ma points to a new phase of upland expansion at the north of the Amazon River in central Amazonia (Fig. 10C). After 18 Ma, renewed floodplain expansion started with the deposition of the Novo Remanso Formation (Fig. 10D). This expansion of the floodplains would also lead to the reorganization of biological communities, with the expansion of flooded environments-adapted taxa through central Amazonia. Interestingly, phases of expansion of floodplains between ~18 and ~ 8 Ma means that upland forests and associated species were more restricted, at least temporally, during this period, due to the deposition of the Novo Remanso Formation in the lower Negro-Solimões interfluve, an area that currently harbors endemic upland forest bird (Borges and Da Silva, 2012) and primate species (Boubli et al., 2015), and is recognized as the Jaú area of endemism (Borges and Da Silva, 2012).

The iron-enrichment levels (i.e., petroplinthite) in the Novo Remanso deposits indicate stable surface under lateritic weathering, which agrees with the establishment of upland forests, i.e. Terra Firme, at the study site for at least 3 Ma (Fig. 10E). In agreement with this scenario, molecular dating based on accumulation of differences in DNA sequences of natural populations (molecular clock) indicates the isolation of upland bird and primate species endemic to the Jaú area of endemism from their sister taxa at the upland forests from the Guiana area of endemism, to the east of the Negro River, during the last 3 Ma (Ribas et al., 2012; Boubli et al., 2015; Crouch et al., 2018; Silva et al., 2019). Among birds, splits associated with the lower Negro River have a mean date between 3 and 1 Ma (Ribas et al., 2012; Silva et al., 2019; Naka and Brumfield, 2018). Among primates, correspondent splits range from 1.8 to 0.8 Ma (Boubli et al., 2015). The establishment of the lower Negro River as a barrier for dispersal of upland forest taxa agrees with our maximum estimate of incision of the lower Negro channel since at least 3 Ma. The shift from floodplains to uplands due to channel incision at the study site described here may help understand this scenario, and the consolidation of the lower Negro River as a biogeographical barrier, with upland forest becoming widespread and long-lasting on opposite margins, which currently correspond to the Jaú and Guiana areas of endemism (Silva et al., 2019) (Fig. 10E). This scenario also corroborates the contrasting characteristics of bird communities observed between the Jaú and Guiana areas of endemism (Crouch et al., 2018). The Guiana communities are phylogenetically overdispersed, meaning that they include taxa that are less phylogenetically related than what would be expected by chance. This is a characteristic of communities that harbor old and young species, and that have been structured over a longer period (Crouch et al., 2018; Webb, 2000). Contrastingly, the Jaú communities are phylogenetically underdispersed, meaning that they include taxa that are more phylogenetically related than what would be expected by chance (Crouch et al., 2018; Webb, 2000). This may be a characteristic of younger communities, which have been assembled in a shorter period (last 3 Ma). This is in agreement with the deposition and weathering history of fluvial deposits of the Novo Remanso Formation, which would represent the substrate of southern portion of the Jaú area of endemism. Finally, phases of base level drop and channel incision during the Pleistocene (Bezerra et al., 2022) would also have facilitated the establishment of the main river courses that keep uplands separated by main biogeographic barriers in central Amazonia (Fig. 10F).

6. Conclusions

The mineralogical and geochronological investigations of iron-lateritic duricrust and iron-enrichment levels developed on ancient fluvial terraces in central Amazonia allow to refine the age of the fluvial sedimentary units and to highlight main phases of upland expansion (alluvial plain retreat) and weathering processes. We demonstrate that the Alter do Chão Formation is older than ~42 Ma, which could host sedimentation during the early Cenozoic. The Iranduba Formation has been deposited before ~30 Ma, suggesting an Oligocene or earlier age while the deposition of the Novo Remanso Formation deposition would occur between 18 and 8 Ma, in agreement with the Miocene age based on pollen data in the literature.

In addition, the iron-lateritic duricrusts and iron-enrichment ages permit to define at least two main weathering phases, with an older phase started around 42 Ma, which was intensified between 30 and 18 Ma, and a younger phase well recorded from ~8 to 1 Ma. During the younger weathering phase, a first precipitation phase of hematite occurred from ~8 to 3 Ma, followed by goethite precipitation from ~3 to 1 Ma. The weathering phases reported in this study suggest that ancient fluvial deposits were recurrently converted into stable uplands in central Amazonia during the Cenozoic, with the youngest recorded conversion ranging from the late Miocene to the late Pliocene or Pleistocene. The younger age is recorded both in iron-lateritic duricrust and iron-enrichment level within the studied deposits is around 1 Ma, suggesting weathering profiles in equilibrium with each other in the study area, where the modern landscape is characterized by incised fluvial channels bounded by fluvial terraces.

Finally, central Amazonian paleo-environments had a significant role for the establishment of biogeographic boundaries in central Amazonia. The temporal coincidence of landscape changes and species diversification presented here is one of the few available multidisciplinary pieces of evidence of a biotic evolution coupled with landscape changes, illustrating fluvial dynamics as a driver of biotic diversification and community assemblage in the most biodiverse region of the world. We also highlight that the landscape changes reconstructed here were probably recurrent and integrate several events at shorter time scales that contributed to originate a major biogeographic boundary such as the lower Negro River.

Funding

This study was supported by the ANR RECA ANR-17-CE01-0012 project and FAPESP funding. M. Albuquerque's salary was funded by the CAPES/COFECUB (French committee for the evaluation of university cooperation with Brazil), process number 88887.284574/2018–00. Fieldwork was funded by the FAPESP grant 2013/03265–5. A.K·K was funded by the Foundation for Support and Evaluation of Graduate Education (CAPES) 88887.370034/2019–00. A.O·S and F.N.P. are funded by CNPq grant #304727/2017–2 and #302411/2018–6, respectively. A.O·S thanks FAPESP grant #2018/23899–2. F.N.P. was supported for a postdoctoral fellowship FAPESP grant #2014/23334–4.

Author contributions

C.G., A.O.S., M.P. and F.N.P. contributed to project planning. C.G., F. N.P., M.P. and S.S. contributed to field survey and sampling. C.G., M.F.d. S.A., S.B.R., C.C., F.H., S.M., J.N., S.S., N.F. and R.P. contributed to the (U-Th)/He, mineralogical and petrological analysis. C.G., A.O.S. and M. P. contributed to financial support. All authors contributed to manuscript and figure preparation.

Declaration of Competing Interest

The authors declare that they have no conflict of interest.

Acknowledgments

We tanked Pierre Burckel is thanked for the access to the ICPMS at IPGP. Zhengtang Guo is thanked for handling the paper submission and Nicholas Perez for the constructive review.

Appendix A. Supplementary data

Supplementary data to this article can be found online at https://doi.

org/10.1016/j.gloplacha.2022.103815.

References

Abinader, H.D., 2008. Estratigrafia de depósitos neógenos da bacia do amazonas, municípios de iranduba e manacapuru, Amazonas, Master dissertation. Universidade Federal do Amazonas, UFAM, Brasil.

Allard, T., Gautheron, C., Bressan-Riffel, S., Balan, E., Selo, M., Fernandes, B.S., Pinna-Jamme, R., Derycke, A., Morin, G., Taitson Bueno, G., Do Nascimento, N.R., 2018. Combined dating of goethites and kaolinites from ferruginous duricrusts. Deciphering the late Neogene erosion history of Central Amazonia. Chem. Geol. 479, 136–150.

Allard, T., Pereira, L., Mathian, M., Balan, E., Taitson Bueno, G., Falguères, C., Do Nascimento, N.R., 2020. Dating kaolinite from the Neogene Içá Formation and overlying laterites, Central Amazonia, Brazil: Constraints for a stratigraphic correlation. Palaeogeogr. Palaeoclimatol. Palaeoecol. 554, 109818.

ANA, 2015. Avaliação dos Aquíferos das Bacias Sedimentares da Província Hidrogeológica Amazonas no Brasil (escala 1:1.000.000) e Cidades Pilotos (escala 1: 50.000). In: Geologia da PHA. v.I.B., Agência Nacional de Águas, 126 pp. (Ed.).

Anderson, V.J., Horton, B.K., Saylor, J.E., Mora, A., Tesón, E., Breecker, D.O., Ketcham, R.A., 2016. Andean topographic growth and basement uplift in southern Colombia: Implications for the evolution of the Magdalena, Orinoco, and Amazon river systems. Geosphere 12, 1235–1256.

Balan, E., Allard, T., Fritsch, E., Sélo, M., Falguères, C., Chabaux, F., P, M.-C., Calas, G., 2005. Formation and evolution of lateritic profiles in the middle Amazon basin: Insights from radiation-induced defects in kaolinite. Geochim. Cosmochim. Acta 69, 2193–2204.

Bertassoli Jr., D.J., Sawakuchi, A.O., Chiessi, C.M., Schefuß, E., Hartmann, G.A., Häggi, C., Cruz, F.W., Zabel, M., McGlue, M.M., Santos, R.A., Pupim, F.N., 2019. Spatiotemporal variations of riverine discharge within the Amazon basin during the late Holocene coincide with extratropical temperature anomalies. Geophys. Res. Lett. 46, 9013–9022.

Bezerra, I.A.A., Nogueira, A.C.R., Motta, M.B., Sawakuchi, A.O., Mineli, T.D., Silva, A.Q., Silva Jr., A.G., Domingos, F.H.G., Mata, G.A.T., Lima, F.L., Riker, S.R.L., 2022. Incision and aggradation phases of the Amazon River in Central-Eastern Amazonia during the late Neogene and Quaternary. Geomorphology 399, 108073.

Bicudo, T.C., Sacek, V., de Almeido, R.P., 2020. Reappraisal of the relative importance of dynamic topography and Andean orogeny on Amazon landscape evolution. Earth Planet. Sci. Lett. 546, 116423.

Borges, S.H., Da Silva, J.M.C., 2012. A new area of endemism for Amazonian Birds in the Rio Negro Basin. The Wilson J. Ornithol. 124, 15–23.

Boubli, J.P., Ribas, C.C., Lynch Alfaro, J.W., Alfredo, M.E., Da Silva, M.N.F., Pinho, G.M., Farias, I.P., 2015. Spatial and temporal patterns of diversification on the Amazon: A test of the riverine hypothesis for all diurnal primates of Rio Negro and Rio Branco in Brazil. Mol. Phylogenet. Evol. 82, 400–412.

Caputo, M.V., 1984. Stratigraphy, Tectonics, Paleoclimatology and Paleogeography of Northern Basins of Brazil. Califórnia University, Santa Barbara, p. 583.

Caputo, M.V., 2009. Discussão sobre a Formação Alter do Chão e o Alto de Monte Alegre. Simpósio de Geologia da Amazônia, Boletim de Resumos Expandidos, Manaus.

Caputo, M.V., Rodrigues, R., Vasconcelos, D.N.N., 1971. Litoestratigrafia da bacia do Amazonas. Petrobras - Sistema de informação de exploração 130 (4054).

Caputo, M.V., Soares, E.A.A., 2016. Eustatic and tectonic change effects in the reversion of the transcontinental Amazon River drainage system. Brazilian J. Geol. 46, 301–328.

Carvalho, M.R., Jaramillo, C., de la Parra, F., Caballero-Rodríguez, D., Herrera, F., Wing, S., Turner, B.L., D'Apolito, C., Romero-Báez, M., Narváez, P., Martínez, C., Gutierrez, M., Labandeira, C., Bayona, G., Rueda, M., Paez-Reyes, M., Cárdenas, D., Duque, A., Crowley, J.L., Santos, C., Silvestro22, D., 2021. Extinction at the end-cretaceous and the origin of modern Neotropical rainforests. Science 372, 63–68.

Cornell, R.M., Schwertmann, U., 2004. The Iron Oxides: Structure, Properties, Reactions, Occurences and Uses, Second edition. Wiley-VCH GmbH&Co, KGaA.

Cracraft, J., Ribas, C.C., d'Horta, F.M., Bates, J., Almeida, R.P., Aleixo, A., Boubli, J.P., Campbell, K.E., Cruz, F.W., Ferreira, M., Fritz, S.C., Grohmann, C.H., Latrubesse, E. M., Lohmann, L.G., Musher, L.J., Nogueira, A., Sawakuchi, A.O., Baker, P., 2020. The origin and evolution of Amazonian species diversity. In: Rull, V. (Ed.), Neotropical diversification: patterns and Processes. Fascinating Life Sciences. Springer, Cham, pp. 225–244.

Crouch, N.M.A., Capurucho, J.M.G., Hackett, S.J., Bates, J.M., 2018. Evaluating the contribution of dispersal to community structure in Neotropical passerine birds. Ecography 42, 390–399.

Cunha, P.R.C., Melo, J.H.G., Silva, O.B., 2007. Bacia do Amazonas. Boletim de Geociências da Petrobras 15, 227–251.

Daemon, R.F., Contreiras, C.J.A., 1971. Zoneamento palinológico da Bacia do Amazonas. In: XXV Congres, Bras. Geol., São Paulo, p. 79e88.

Danišík, M., Evans, N.J., Ramanaidou, E.R., McDonald, B.J., Mayers, C., McInnes, B.I.A., 2013. (U–Th)/he chronology of the Robe River channel iron deposits, Hamersley Province, Western Australia. Chem. Geol. 354, 150–162.

Dino, R., Silva, O.B., Abrahão, D., 1999. Caracterização palinológica e estratigráfica de estratos cretáceos da Formação Alter do Chão, Bacia do Amazonas. In: Claro, B.D.R. E. Rio (Ed.), Simpósio sobre o Cretáceo do Brasil, pp. 557–565.

Dino, R., Amaral Soares, E.A., Antonioli, L., Riccominni, C., Rodrigues Nogueira, A.C., 2012. Palynostratigraphy and sedimentary facies of Middle Miocene fluvial deposits of the Amazonas Basin, Brazil. J. S. Am. Earth Sci. 34, 61–80.

Eze, P.N., Udeigwe, T.K., Meadows, M.E., 2014. Plinthite and its Associated Evolutionary Forms in Soils and Landscapes: A Review. Pedosphere 24, 153–166.

Farley, K.A., 2002. (U-Th)/He dating: Techniques, calibrations, and applications. In: Geochemistry, R.I.M. (Ed.), Noble Gases in Geochemistry and Cosmochemistry, pp. 819–844.

Farley, K.A., 2018. Helium diffusion parameters of hematite from a single-diffusion-domain crystal. Geochim. Cosmochim. Acta 231, 117–129.

Figueiredo, J.P., Hoorn, C., van der Venn, P., Soares, E., 2009. Late Miocene onset of the Amazon River and the Amazon deep-sea fan: evidence from the Foz do Amazonas Basin. Geology 37, 619–622.

Gautheron, C., Pinna Jamme, R., Derycke, A., Ahadi, F., Sanchez, C., Haurine, F., Monvoisin, G., Barbosa, D., Delpech, G., Maltese, J., Sarda, P., Tassan-Got, L., 2021. Technical note: Analytical protocols and performance for apatite and zircon (U–Th)/he analysis on quadrupole and magnetic sector mass spectrometer systems between 2007 and 2020. Geochronology 3, 351–370.

Guimarães, J.T.F., Nogueira, A.C.N., Da Silva Jr., J.B.C., Soares, J.L., Alves, R., Kern, A. K., 2015. Palynology of the middle Miocene-Pliocene Novo Remanso formation, Central Amazonia. Brazil Ameghinaiana 52, 107–134.

Guinoiseau, D., Fekiacova, Z., Allard, T., Druhan, J.L., Balan, E., Bouchez, J., 2021. Tropical weathering history recorded in the silicon isotopes of lateritic weathering profiles. Geophys. Res. Lett. 49, 1–11.

Heller, B.M., Bressan-Riffel, S., Allard, T., Morin, G., Roig, J.-Y., Couëffe, R., Derycke, A., Ansart, C., Pinna Jamme, R., Gautheron, C., 2022. Reading the climate signals hidden in bauxite. Geochim. Cosmochim. Acta 323, 40–73. https://doi.org/10.1016/j.gca.2022.02.017.

Hofmann, F., Reichen, B., Farley, K.A., 2017. Evidence for >5Ma paleo-exposure of an Eocene–Miocene paleosol of the Bohnerz Formation, Switzerland. Earth Planet. Sci. Lett. 465, 168–175.

Hoorn, C., Bogota-A, G.R., Romero-Baez, M., Lammertsma, E.I., Flantua, S.G.A., Dantas, E.L., Dino, R., do Carmo, D.A., Chemale Jr., F., 2017. The Amazon at sea: Onset and stages of the Amazon River froma marine record, with special reference to Neogene plant turnover in the drainage basin. Glob. Planet. Chang. 153, 51–65.

Junk, W.J., Piedade, M.T.F., Schöngart, J., Cohn-Haft, M.A., J.M. and Wittmann, F., 2011. A classification of major naturally-occurring Amazonian lowland wetlands. Wetlands 31, 623–640.

Ketcham, R.A., Gautheron, C., Tassan-Got, L., 2011. Accounting for long alpha-particle stopping distances in (U-Th-Sm)/he geochronology: refinement of the baseline case. Geochim. Cosmochim. Acta 75, 7779–7791.

Mapes, R., 2009. Past and Present Provenance of the Amazon River. University of North Carolina, Chapel Hill, p. 185.

Martínez, C., Jaramillo, C., Correa-Metrío, A., Crepet, W., Moreno, J.E., Aliaga, A., Moreno, F., Ibañez-Mejia, M., Bush, M.B., 2020. Neogene precipitation, vegetation, and elevation history of the Central Andean Plateau. Sci. Adv. 6, eaaz4724.

McCusker, L.B., Von Dreele, R.B., Louer, D., Scardi, P., 1999. Rietveld Refinement Guidelines. J. Appl. Crystallogr. 32, 36–50.

Mendes, A.C., Salomao, G.N., Nogueira, A.C.R., Dantas, E.L., 2015. Provenance of the Alter do Chão Formation in Amazonas State (Itacoatiara-Parintins Cities), Amazonas Basin, Brazil, XV. In: Congresso Brasileiro de Geoquímica - International Symposium on Climate and Geodynamics of Amazon Basin, Brasília.

Monteiro, H., Vasconcelos, P.M., Farley, K.A., Spier, C.A., Mello, C.L., 2014. (U-Th)/he geochronology of goethite and the origin and evolution of Cangas. Geochim. Cosmochim. Acta 131, 267–289.

Mora, A., Parra, M., Strecker, M.R., Sobel, E.R., Hooghiemstra, H., Torres, V., Jaramillo, J.V., 2008. Climatic forcing of asymmetric orogenic evolution in the Eastern Cordillera of Colombia. Geol. Soc. Am. Bull. 120, 930–949.

Nahon, D., 2003. Weathering in tropical zone. Significance through ancient and still active mechanisms. C. R. Geosci. 335, 1109–1119.

Nahon, D., Tardy, Y., 1992. Chapter I.3 - the ferruginous laterites. Handb. Explor. Geochem. 4, 41–55.

Naka, L.N., Brumfield, R.T., 2018. The dual role of Amazonian rivers in the generation and maintenance of avian diversity. Sci. Adv. 4, eaar8575.

Nobre, C.A., Sellers, P.J., Shukla, J., 1991. Amazonian deforestation and regional climate change. J. Clim. 4 (10), 957–988.

Parra, M., Mora, A., Jaramillo, C., Torres, V., Zeilinger, G., Strecker, M.R., 2010. Tectonic controls on Cenozoic foreland basin development in the North-Eastern Andes, Colombia. Basin Res. 22, 874–903.

Pupim, F.N., Sawakuchi, A.O., Almeida, R.P., Ribas, C.C., Kern, A.K., Hartmann, G.A., Chiessi, C.M., Tamura, L.N., Mineli, T.D., Savian, J.F., Grohmann, C.H., Bertassoli Jr., D.J., Stern, A.G., Cruz, F.W., Cracraft, J., 2019. Chronology of Terra Firme formation in Amazonian lowlands reveals a dynamic Quaternary landscape. Quat. Sci. Rev. 210, 154–163.

Retallack, G.J., 2010. Lateritization and Bauxitization events. Econ. Geol. 105, 655–667.

Ribas, C.C., Aleixo, A., Nogueira, A.C., Miyaki, C.Y., Cracraft, J., 2012. A palaeobiogeographic model for biotic diversification within Amazonia over the past three million years. Proc. Biol. Sci. 219, 681–689.

Riffel, S.B., Vasconcelos, P.M., Carmo, I.O., Farley, K.A., 2016. Goethite (U–Th)/he geochronology and precipitation mechanisms during weathering of basalts. Chem. Geol. 446, 18–32.

Rozo, J.M.G., Nogueira, A.C.R., Horbe, A.M.C., Carvalho, A.S., 2005. Depósitos neógenos da Bacia do Amazonas. In: Horbe, A.M.C., Souza, V.S. (Eds.), Contribuições a Geologia da Amazônia. SBG, Manaus.

Sacek, V., 2014. Drainage reversal of the Amazon River due to the coupling of surface and lithospheric processes. Earth Planet. Sci. Lett. 401, 301–312.

Shephard, G.E., Müller, R.D., Liu, L., Gurnis, M., 2010. Miocene drainage reversal of the Amazon River driven by plate–mantle interaction. Nature Geo. 3, 870–975.

Shobbenhauns, C., Bellizzia, A., 2001. Geological Map of South America, 1:5.000.000, in: UNESCO, C.C.D. (Ed.), Brasilia.

Shuster, D., Vasconcelos, P., Heim, J., Farley, K.A., 2005. Weathering geochronology by (U-Th)/he dating of goethite. Geochim. Cosmochim. Acta 69, 659–673.
Silva, S.M., Peterson, A.T., Carneiro, L., Burlamaqui, T.C.T., Ribas, C.C., Sousa-Neves, T., Miranda, L.S., Fernandes, A.M., d'Horta, F.M., Araújo-Silva, L.E., Bandeira, C.H.M. M., Dantas, S.M., Ferreira, M., Martins, D.M., Oliveira, J., Rocha, T.C., Sardelli, C.H., Thom, G., Rêgo, P.S., Santos, M.P., Sequeira, F., Vallinoto, M., Aleixo, A., 2019. A dynamic continental moisture gradient drove Amazonian bird diversification. Sci. Adv. 5, eaat5752.
Soares, E.A.A., Dino, R., Soares, D.P., Antonioli, L., da Silva, M.A.L., 2015. New sedimentological and palynological data from surface Miocene strata in the Central Amazonas Basin area. Brazilian. J. Geol. 45.
Tardy, Y., 1992. Pétrologie des latérites et des sols tropicaux.
Tassinari, C.C.G., Macambira, M.J.B., 1999. Geochronological provinces of the Amazonian craton. Episodes 22, 174–182.
Thom, G., Xue, A.T., Sawakuchi, A.O., Ribas, C.C., Hickerson, M.J., Aleixo, A., Miyaki, C., 2020. Quaternary climate changes as speciation drivers in the Amazon floodplains. Sci. Adv. 6, eaax4718.
Vasconcelos, P.M., Heim, J.A., Farley, K.A., Monteiro, H., Waltenberg, K., 2013. $^{40}Ar/^{39}Ar$ and (U–Th)/he – $^{4}He/^{3}He$ geochronology of landscape evolution and channel iron deposit genesis at Lynn Peak, Western Australia. Geochim. Cosmochim. Acta 117, 283–312.
Vasconcelos, P.M., Reich, M., Shuster, D., 2015. The paleoclimatic signatures of supergene metal deposits. Elements 11, 317–322.
Vermeesch, P., 2009. RadialPlotter: A Java application for fission track, luminescence and other radial plots. Radiat. Meas. 44, 409–410.
Vermeesch, P., 2010. HelioPlot, and the treatment of overdispersed (U-Th-Sm)/he data. Chem. Geol. 271, 108–111.
Wallace, A.R., 1852. On the monkeys of the Amazon. Proc. Zool. Soc. London 20, 107–110.
Webb, C.O., 2000. Exploring the phylogenetic structure of ecological communities: an example for rain forest trees. Am. Nat. 156, 145–155.
Westerhold, T., Marwan, N., Drury, A.J., Liebrand, D., Agnini, C., Anagnostou, E., Barnet, J.S.K., Bohaty, S.M., Vleeschouwer, D.D., Florindo, F., Frederichs, T., Hodell, D.A., Holbourn, A.E., Kroon, D., Lauretano, V., Littler, K., Lourens, L.J., Lyle, M., Pälike, H., Röhl, U., Tian, J., Wilkens, R.H., Wilson, P.A., Zachos, J.C., 2020. An astronomically dated record of Earth's climate and its predictability over the last 66 million years. Science 369, 1383–1387.
Zachos, J.C., Pagani, M., Sloan, L., Thomas, E., Billups, K., 2001. Trends, rhythms, and aberrations in global climate 65 Ma to present. Science 292, 686–693.
Zhao, L., Hong, H., Fang, Q., Yin, K., Wang, C., Li, Z., Torrent, J., Cheng, F., Algeo, T.J., 2017. Monsoonal climate evolution in southern China since 1.2 Ma: New constraints from Fe-oxide records in red earth sediments from the Shengli section, Chengdu Basin. Paleogeogr. Paleoclimatol. Paleoecol 473, 1–15.